



LUND UNIVERSITY
Faculty of Science

Vanadium-based neutron-beam monitor

Vendula Maulerová

Thesis submitted for the degree of Master of Science
Project duration: 18 months, 60 hp

Supervised by Kevin Fissum and Fatima Issa

Department of Physics
Division of Nuclear Physics
May, 2019

Abstract

A prototype invasive (quasi-parasitic) thermal-neutron beam monitor based on isotropic neutron scattering from a thin natural Vanadium foil and standard ^3He proportional counters has been conceptualized, designed, simulated, calibrated, and commissioned. As the beam monitor is invasive, very low neutron-beam attenuation is a necessary characteristic. Further, response linearity over as wide a range of rates as possible is highly desirable. The prototype was first calibrated using radioactive neutron sources at the Source-Testing Facility at the Division of Nuclear Physics in Lund, Sweden. Subsequently, the prototype was commissioned with beams of neutrons at the V17 and V20 beamlines of the Helmholtz Zentrum in Berlin, Germany. Both low attenuation and response linearity have been successfully demonstrated, indicating the concept is viable and worth continued development efforts. In this thesis, a monographic overview of the development of the prototype is presented.

Acknowledgements

The completion of this thesis would not have been possible without a large number of people that have contributed with valuable assistance and support.

I would like to express my sincere gratitude to my supervisor Kevin Fissum for his patient guidance, feedback and support during all stages of my master thesis related work. Thank you for all your enthusiasm and encouragement during the experimental stages, for your valuable insights when evaluating the simulations and for all your language lessons during the writing stage. Most of all thank you for showing me that values like empathy, loyalty and fair-play are the most important part of becoming a scientist.

Furthermore I wish to express my sincere thanks to Kalliopi Kanaki, who was never too tired to hear any question related to Geant4 simulations and the ESS framework and later accompanied me for the measurements at HZB, Berlin. Thank you for all your support and thank you for your determined and uplifting spirit during all those long hour days in Berlin.

To Richard Hall-Wilton, thank you for giving me the opportunity to work on a project, that allowed me to apply the knowledge gained at the university to the real world product. Thank you for always going out of your way in order to make this project possible financially and timewise and for all your valuable feedback provided during the writing phase.

To Fatima Issa, my co-supervisor, I would like to thank for introducing me to beam monitors and giving me the initial idea about the possibilities and limitations of the project.

I would especially like to thank all the members of the SONNIG group at Lund University: thank you for creating an atmosphere in which I always felt comfortable when expressing my thoughts, opinions and ideas. Thank you for giving me valuable feedback and encouragement at all times. I would especially like to thank Nicholai Mauritzson, who is the most hands-on person I have ever met. Thank you for being always ready to give me a hand when it comes to drilling, welding, soldering and 3D printing. Thank you for giving me ideas on my detector setup and most of all thank you for being my friend from the day I came to the Source-Testing Facility (STF) until now.

To Rasmus Kjær Høier, it was a pleasure to share office with you! During last year and half you became my dear friend. Thank you for all the moments of misery and glory we could share together.

My gratitude goes also to the entire Detector Group at European Spallation Source (ESS). I have never worked in an environment with people from such different backgrounds! Thank you all for your interesting insights with respect to the master thesis. Namely I would like to thank to Francesco Piscitelli for his knowledge and expertise when it comes to electronics. I would like to thank Irina Stefanescu for all the straight-to-the point advices whenever I wasn't sure about detectors. I would like to thank Common Beam Monitor project members: Steven Alcock and Ioannis Apostolidis for helping the implementation of my project to the actual ESS beam-lines. To Alessio Laloni, thank you for all the help at the Utgård workshop.

Financially, this project would not be possible without the financial support from BrightnESS, EU, H2020 grant number: 676548. I would also like to acknowledge the support from Helmholtz-Zentrum Berlin with a special attention to Peter Kadletz, Robin Woracek and Thomas Wilpert for all the help during the experiments.

Finally, I would like to show my love to all my non-physicist friends, who were always ready to make my worries disappear during darker times and ready to share my happiness during times I made progress. I would like to thank my family, especially to my brothers, who were always ready to call me at the midnight when the times were difficult. I know that you took on your shoulders so many things last year! I would have never finished my thesis if it weren't for Matěj Mauler who took charge when the rest of our family could not. To my sister: thank you so much for your enormous will when you fought so much harder and bigger problems. Thank you that

you never gave up and that you despite your never-ending physical pain, you have always found out a courage to support me even though I had been so far away. Your living will is a continuous inspiration for me!

Contents

Abstract	i
Acknowledgments	iii
List of Figures	vii
List of Tables	ix
Abbreviations	xi
1 Overview	1
1.1 Introduction	1
1.2 Motivation	2
1.2.1 Concept	2
1.2.2 Material	4
1.2.3 Monitoring approaches	4
1.3 Goal	6
2 Calibrations at the Source-Testing Facility	7
2.1 Facility overview	7
2.2 Apparatus	7
2.2.1 Radioactive sources	7
2.2.2 Moderator	9
2.2.3 Vanadium foils	12
2.2.4 Detectors	12
2.2.5 Data-acquisition system	16
2.3 Measurements and analysis	18
2.3.1 Absorption	18
2.3.2 Scattering	22
2.4 Results	24
2.4.1 Absorption	24
2.4.2 Scattering	26
2.5 Summary	27
3 Commissioning at Helmholtz-Zentrum Berlin	29
3.1 Facility overview	29
3.2 Apparatus	29
3.2.1 Beamlines	29
3.2.2 Data-acquisition system	30
3.3 Measurements and analysis	32
3.4 Results	36
3.4.1 V17	36
3.4.2 V20	37
3.5 Summary	39
4 Closing Remarks	41
4.1 Summary	41
4.2 Conclusions	42
4.3 Outlook	42
A ^3He Detector Studies	i
A.1 Shaping Time and resolution	i
A.2 Simulated response	iii

List of Figures

1.1	Overview of the European Spallation Source.	2
1.2	Beam-monitor requirements at the European Spallation Source.	3
1.3	Isotropic invasive beam-monitor concept.	3
1.4	Neutron attenuation versus ^{nat}V thickness at 1.8 \AA	4
1.5	Neutron absorption cross section versus wavelength for ^{51}V	5
1.6	Thermal-neutron capture and β^- decay.	5
1.7	Neutron capture on ^{51}V	5
1.8	Neutron scattering from ^{51}V	6
2.1	Overview of the Source-Testing Facility.	7
2.2	Decay schemes of the γ -ray sources.	8
2.3	Simplified decay scheme of ^{241}Am	8
2.4	Geant4 $^{241}\text{Am}/^9\text{Be}$ neutron simulation.	9
2.5	The neutron thermalizer.	11
2.6	$^{241}\text{Am}/^9\text{Be}$ neutron simulations before and after thermalization.	11
2.7	Photograph of ^{nat}V rod and foils.	12
2.8	Schematic overview of a scintillation detector.	13
2.9	Photographs of the $\text{LaBr}_3:\text{Ce}$ and CeBr_3 detectors.	14
2.10	Response of a scintillation detector to a monoenergetic γ -rays.	14
2.11	An illustration of energy resolution.	15
2.12	Response of a ^3He detector to thermal neutrons.	16
2.13	Schematic overview of a ^3He detector.	16
2.14	Photograph of the ^3He detector.	17
2.15	Data-acquisition system for the CeBr_3 detector.	17
2.16	Data-acquisition system for the ^3He and $\text{LaBr}_3:\text{Ce}$ detectors.	18
2.17	Activation of the ^{nat}V samples as a function of time.	19
2.18	Setup for the activation of ^{nat}V	20
2.19	Setup for the activated ^{nat}V de-excitation γ -ray measurements.	20
2.20	The de-excitation γ -ray analysis.	21
2.21	The de-excitation γ -ray analysis cross check.	22
2.22	Setup for the ^{nat}V neutron-scattering measurements.	23
2.23	The neutron-scattering analysis.	24
2.24	γ -ray spectra from activated ^{nat}V	25
2.25	Time constant of the activated ^{nat}V decay.	26
2.26	Neutron scattering on ^{nat}V	27
3.1	Overview of the BER II reactor at Helmholtz-Zentrum Berlin.	29
3.2	Layout of V20.	30
3.3	DAQ system for the ^3He detectors.	30
3.4	Fission chamber from LND	31
3.5	Fission-chamber response.	31
3.6	Setup for the ^{nat}V neutron-scattering measurements.	32
3.7	Beamline at V17.	33
3.9	Beamline at V20.	34
3.8	The analysis of the V17 data.	34
3.10	The analysis of the V20 data.	35
3.11	Prototype beam-monitor results for V17.	36

3.12	Chopper phase-angle opening and neutron-beam intensity.	37
3.13	Prototype beam-monitor results for V20.	38
3.14	Absorption and scattering cross section extracted from the V20 data.	39
A.1	Shaping-time analysis.	i
A.2	Full-deposition peak as a function of shaping time.	ii
A.3	Resolution of the full-deposition peak as a function of shaping time.	ii
A.4	Response of the ^3He detector.	iii
A.5	Energy-resolution smeared response of the ^3He detector.	iv
A.6	Visualization of the ^3H and ^1H trajectories inside the ^3He detector.	iv
A.7	Stopping powers of ^3H s and ^1H s in the ^3He	v
A.8	Illustration of the custom-response algorithm.	vi
A.9	Simulation-smeared response of the ^3He detector.	vii

List of Tables

2.1	γ -ray sources and their characteristic energies.	8
2.2	Maximum energy transfer as a function of A.	10
2.3	Fundamental properties of ^{nat}V	12
2.4	^{nat}V foil dimensions and calculated attenuations.	12
2.5	Scintillation properties of $\text{LaBr}_3\text{:Ce}$ and CeBr_3 crystals.	13
2.6	Overview of the data-acquisition systems.	18
2.7	Parameters for ^{nat}V activation calculations.	19
2.8	$^{nat}\text{V}^*$ de-excitation data sets.	19
2.9	Neutron-scattering measurements on the ^{nat}V foils.	23
2.10	The decay constant for the de-excitation of $^{nat}\text{Cr}^*$	26
3.1	Neutron-scattering measurements at V17.	33
3.2	Slit openings and the corresponding flux.	33
3.3	Neutron-scattering measurements at V20.	35
3.4	Theoretical neutron attenuation in ^{nat}V at V17.	36
3.5	Measured neutron attenuation in ^{nat}V at V20.	39

List of Abbreviations

ESS	European Spallation Source
ERIC	European Research Infrastructure Consortium
LINAC	linear accelerator
BM	beam monitors
DG	Detector Group
TOF	time-of-flight
MCA	multi-channel analyzer
STF	Source-Testing Facility
DAQ	data-acquisition system
PMT	photomultiplier tube
FWHM	full-width-at-half-maximum
CERN	Conseil Européen pour la Recherche Nucléaire
HZB	Helmholtz=Zentrum Berlin
BL	beamlines
RoI	region-of-interest
Fg	foreground
Bg	background
NIM	Nuclear Instrumentation Module
Geant4	for GEometry ANd Tracking
HV	High Voltage

1 Overview

1.1 Introduction

Chargeless neutrons are excellent probes of matter. Neutron-imaging techniques are generally viewed as complementary to photon-imaging techniques as neutrons are more sensitive to low- A elements such as hydrogen, lithium, boron, carbon, and nitrogen while photons are more sensitive to high- A elements such as iron and other metals. In particular, neutrons with wavelengths on the order of atomic dimensions ($\sim 1 \text{ \AA}$, $1.8 \text{ \AA} = 25 \text{ meV}$) are especially useful. Neutron-imaging techniques are presently being used in medicine (to characterize soft tissues), biology (to characterize various proteins and DNA structures), archeology (to analyze the internal structure of irreplaceable items without damage) and in material science (to characterize novel materials) to name a few.

The European Spallation Source (ESS), currently under construction in Lund, Sweden, is envisioned to lead worldwide efforts in the field of neutron science for the next 50 years. To be completed in 2025, ESS is a European Research Infrastructure Consortium (ERIC) established to design, construct and commission a multi-disciplinary facility based upon a unique neutron source. This neutron source originates from spallation¹ when a 2.86 ms, 14 Hz pulsed 2 GeV proton beam strikes a thick tungsten target. The peak neutron flux will be $\sim 30\times$ higher than the peak neutron flux from any existing reactor source and $\sim 5\times$ higher than the flux from any existing spallation source [1, 2]. Moderators together with beam shapers (known as choppers [3]) and neutron guides will be used to vary the energy and the energy-spread characteristics of these neutron pulses delivered to the various instrument stations. Due to the high integrated flux and the unique time structure of the neutron pulses, instrument stations will receive neutron beams with rates and wavelengths never before available. This is in turn anticipated to facilitate new research in nanotechnology, medicine, material sciences, environmental sciences and other disciplines.

¹Spallation occurs when a nucleus bombarded with highly energetic protons (for example), is fragmented into multiple particles (spall) including many neutrons.

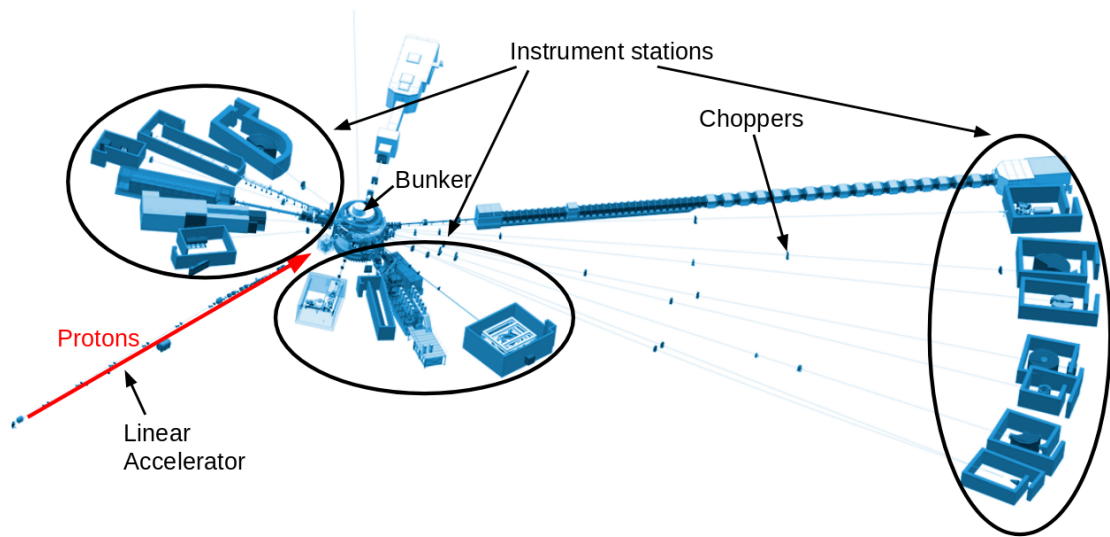


Figure 1.1. Overview of the European Spallation Source. A linear accelerator directs the proton beam (red arrow) towards a tungsten target located in the bunker. Neutrons are created via spallation and moderated and guided to instrument stations. Choppers located along the instrument beamlines are used to define the wavelength and flux for each of the instrument stations individually. Adapted from Ref. [4].

Figure 1.1 shows the planned layout of ESS. The linear accelerator (LINAC) accelerates protons to an energy of 2 GeV and directs them towards the tungsten target, where spallation results in the production of large numbers energetic neutrons. A heavily shielded bunker contains the intense radiation field created as a byproduct of this neutron production. Moderators and beamguides will be used to select the appropriate neutron phase space to be directed towards a given sample in a given instrument station. Choppers will be used to select the neutron energy for each instrument station. In order to verify the alignments, fluxes and energies of the beams, beam monitors (BM)s will be placed in the bunker and along the instrument beamlines (BL)s. The subject of this thesis is the development of one such BM technology.

1.2 Motivation

ESS instrument BLs must reliably transfer neutrons from the bunker to the instrument stations. Reliable transfer requires precision monitoring of the neutron beams using well-understood BMs located at crucial points along the BLs. Figure 1.2 presents an overview of the BMs required at ESS. In general, a BM must be able to withstand very high neutron fluxes and must not appreciably disturb the beam it is monitoring.

1.2.1 Concept

The basic requirement for an invasive² BM is that it disturbs the beam as little as possible. This generally requires having as little material in the beam as possible. Further, a material with neutron-interaction properties resulting in an easily identifiable signal is highly desirable.³ Finally, response linearity over a wide range of rates is advantageous.

Figure 1.3 shows the basic design of an isotropic BM.⁴ A thin foil is placed in a beam of

²Invasive beam monitoring means that the monitor affects the beam continuously. It may not be removed.

³Other properties of interest for the base material for an invasive BM include radiation hardness, vacuum tolerance, and that the material isotropically scatters neutrons. Note that few materials scatter thermal neutrons isotropically.

⁴This design has been inspired by a similar device at the ISIS Neutron and Muon Source at the STFC Rutherford Appleton Laboratory near Oxford, UK [6, 7].



Figure 1.2. Beam-monitor requirements at the European Spallation Source. The pie chart shows the monitor distribution. The BM investigated in this thesis corresponds to the red and green pie slices and has the specifications given in the red rectangle. Adapted from [5].

neutrons and in the ideal case only a very small fraction of the incident neutrons interact by scattering or being captured by the foil. The detector type and size as well as the distance from the edge of the foil to the detectors must be optimized to ensure that the detectors do not become saturated. Their geometrical acceptance and detection efficiency must be large enough to measure the flux from the scattering or absorption reactions in the foil. The setup may then be calibrated to provide a monitor of the beam flux incident on the foil. Symmetrically arranged detector elements have advantages. For example, in normal operation mode, each detector will count at the same rate if the beam is centered between them. An increase in rate in one of the detectors may thus indicate a non-isotropic distribution of the beam.

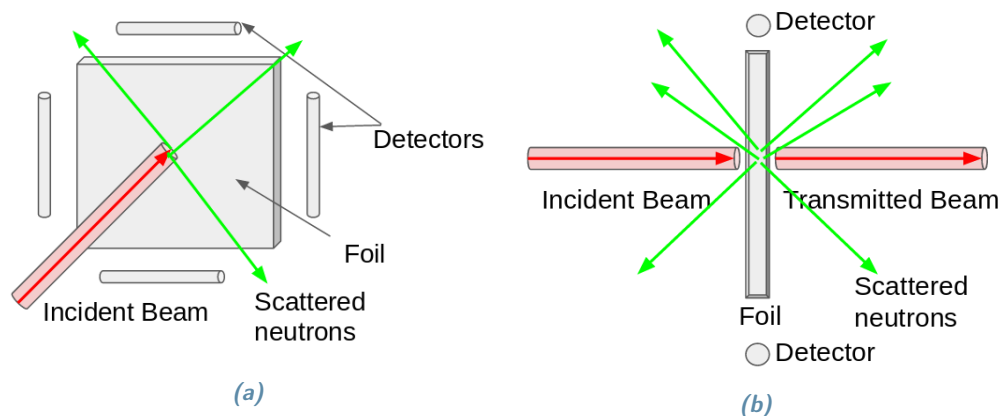


Figure 1.3. Isotropic invasive beam-monitor concept. A thin foil (blue square) is placed in the beam of neutrons (the red arrow). A very small fraction of neutrons (green arrows) are scattered from the foil into the detectors. (a) Quasi-oblique frontal view (b) Top view.

1.2.2 Material

It is well known that ^{nat}V is both robust and radiation hard [8,9].⁵ ^{nat}V is also vacuum tolerant and is one of few materials known to scatter neutrons elastically⁶ and incoherently, i.e. isotropically. In fact, next to hydrogen, only ^{nat}V scatters isotropically [9–13]. ^{nat}V is thus an excellent choice for an invasive BM.

Consider a neutron beam with flux Φ_{beam} . The total disturbance of the incident neutron beam R is given by

$$R = \frac{\Phi_{\text{disturbed}}}{\Phi_{\text{beam}}} = (1 - e^{-n \cdot \sigma \cdot z}), \quad (1.2.1)$$

where $\Phi_{\text{disturbed}}$ is the number of beam neutrons lost to capture or scattering, n is the number density of ^{nat}V , σ is the total interaction cross section⁷ and z is the thickness of the material in the direction of the beam. Figure 1.4 presents R as a function of the thickness z of a ^{nat}V foil. The trend is exponential for $\sim\text{mm}$ thicknesses and linear for $\sim\mu\text{m}$ thicknesses. The inset illustrates that thicknesses less than $150 \mu\text{m}$ ⁸ will disturb less than 1% of the beam, a desirable characteristic for an invasive (quasi-parasitic) beam-monitor.

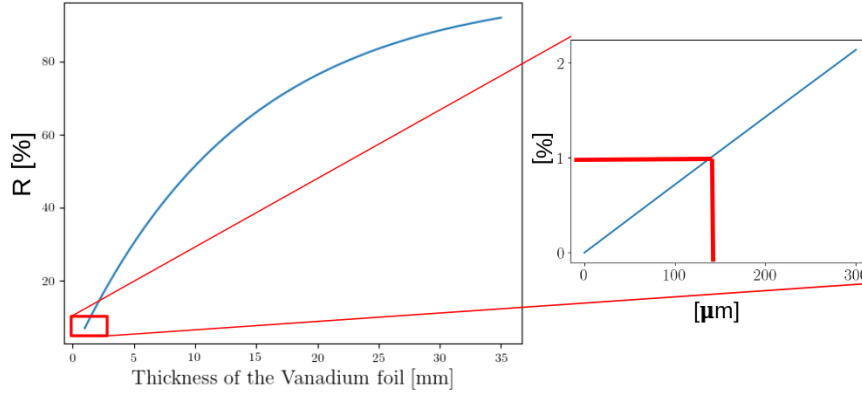


Figure 1.4. Neutron attenuation versus ^{nat}V thickness at 1.8 \AA . The inset demonstrates that for thicknesses below $130 \mu\text{m}$, the foil disturbs less than 1% of the beam.

1.2.3 Monitoring approaches

The detectors shown in Fig. 1.3 must be chosen to match the interaction between the beam and the foil being investigated. Two particularly useful methods which may be exploited to monitor neutron beams are absorption and scattering. Neutron absorption may lead to the emission of a γ -ray, and thus, γ -ray detectors must be employed. Similarly, neutron scattering requires neutron detectors. The underlying monitoring approaches are fundamentally different.

Absorption-based BM

A BM based on neutron capture by ^{nat}V must detect γ -rays released during the post-absorption de-excitation process. The cross section for neutron absorption (capture) at 1.8 \AA (25 meV) is 5.08 b. Figure 1.5, generated using the ESS/Geant4 framework [18] and NCrystal project [19], shows the dependence of $\sigma_{\text{absorption}}$ on the wavelength of the neutron.

⁵ ^{nat}V is a mixture of ^{51}V (99.75%) and ^{50}V (0.25%).

⁶ Elastic scattering is an important consideration if the BM is to provide monitoring of the energy of the beam.

⁷ The cross section reported in Refs. [14–16] has been used for the calculation.

⁸ ^{nat}V foils with thicknesses $125 \mu\text{m}$, $40 \mu\text{m}$ and $20 \mu\text{m}$ are currently available [17].

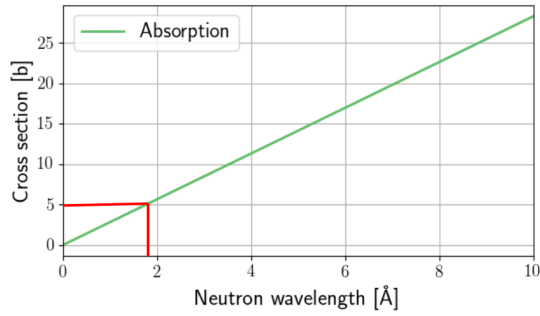


Figure 1.5. Neutron absorption cross section versus wavelength for ^{51}V . At 1.8 \AA , the cross section is 5.08 b .

The capture process is given by:

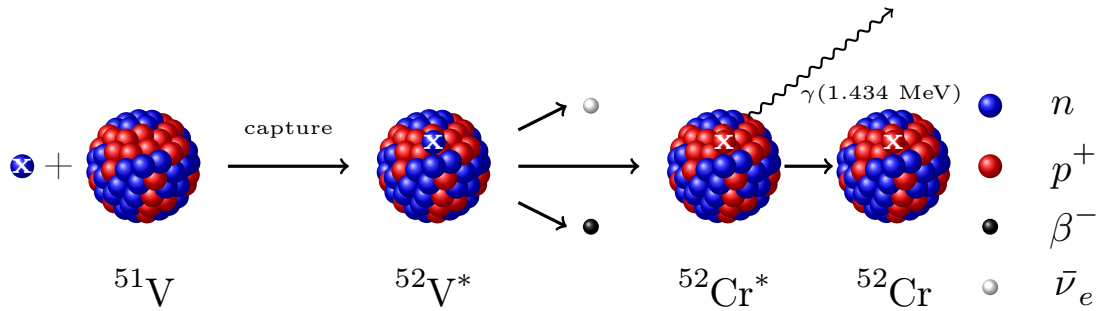
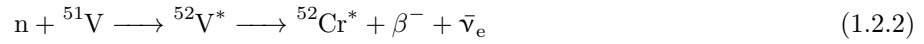


Figure 1.6. Thermal-neutron capture and β^- decay. From left: the thermal neutron is captured by the ^{51}V nucleus. $^{52}\text{V}^*$ with half-life 225 s β^- decays into the first excited state of $^{52}\text{Cr}^*$ which de-excites by releasing a 1.434 MeV γ -ray.

Figure 1.6 shows a diagrammatic representation of neutron capture on ^{51}V . After the neutron is captured, $^{52}\text{V}^*$ is produced, which then β^- decays to $^{52}\text{Cr}^*$ with a branching ratio of unity and half-life of 225 s . Figure 1.7 shows a level-scheme representation of the β^- decay process followed by the $^{52}\text{Cr}^*$ de-excitation in more detail. Over 99% of $^{52}\text{Cr}^*$ nuclei will be in the first excited state, eventually decaying and emitting a 1.434 MeV γ -ray. This 1.434 MeV γ -ray can be used as the signature of neutron capture and thus as a monitor of the beam.

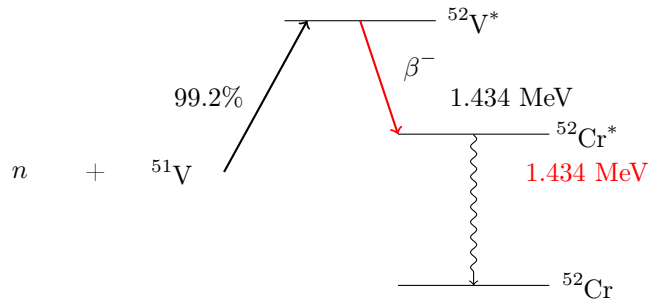


Figure 1.7. Neutron capture on ^{51}V . The 1.434 MeV γ -ray results from the de-excitation of the first excited state of $^{52}\text{Cr}^*$.

Scattering-based BM

Neutron elastic scattering has two components: coherent and incoherent. Coherent (Bragg) scattering is essentially a measure of the interference between the waves of the neutrons scattered by the nuclei of the surrounding atoms. A strong interference pattern may result. The orderliness of the pattern will increase with the increasing orderliness of the crystal of the target material. Incoherent scattering means no interference occurs between the neutron waves scattered from surrounding nuclei.

For ^{nat}V , the neutron-scattering cross sections at 1.8 Å are $\sigma_{\text{incoherent}} = 5.08$ b and $\sigma_{\text{coherent}} = 0.0184$ b, respectively [14–16]. The cross section for each of the reactions is energy dependent. Figure 1.8 demonstrates this energy dependence and was generated again using ESS /Geant4 framework and NCrystal project. Incoherent elastic scattering clearly dominates, as evidenced by the negligible coherent cross section⁹ and the lack of structure in the phase space plot.

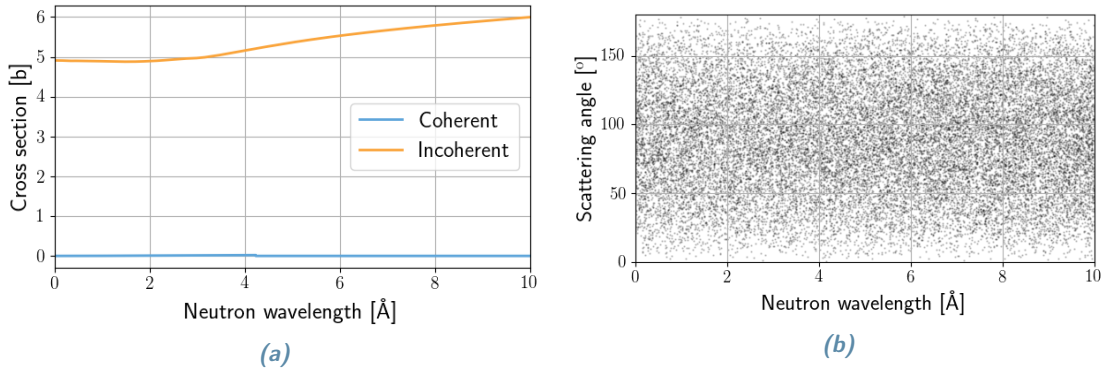


Figure 1.8. Neutron scattering from ^{51}V . (a) Cross section versus wavelength. (b) Simulated scattering angle as a function of wavelength. The lack of features in the scatterplot indicates an isotropic phase space.

In either case, the size of the active area of the detectors A and the distance r from the center of the ^{nat}V foil must be optimized as a function of neutron beam flux. The main consideration for the optimization is the range of fluxes incident on the detector surface. It should be large enough to be detectable but small enough not to saturate the detector. The range of fluxes for which the detector performs well is usually provided by the manufacturer. Optimization leads to:

$$\Phi_{\text{detected}} = \frac{\sigma_i}{4\pi} \frac{A}{r^2} \cdot n \cdot z \cdot \Phi_0 = 0.00358 \cdot \frac{A}{r^2} \cdot \Phi_0 \quad (1.2.4)$$

$$\text{LDR} < 0.00358 \cdot \frac{A}{r^2} \cdot \Phi_0 < \text{HDR} \quad (1.2.5)$$

where n is the number density $n = 7.09 \cdot 10^{22} \text{ cm}^{-3}$ for ^{nat}V , Φ_0 the initial flux, σ_i is the the cross section (for absorption in the case of γ -ray detectors and for scattering in the case of neutron detectors), z is the thickness of the ^{nat}V foil (in this case 125 μm) and LDR and HDR denote the lowest detectable rate and the highest detectable rate, respectively.

1.3 Goal

The goal of this thesis is to investigate the feasibility of an invasive (quasi-parasitic)¹⁰ BM based upon ^{nat}V for beam diagnostics at high flux BLs at spallation sources in close proximity to choppers. The project was carried out in collaboration with the Detector Group (DG) of ESS as a part of the Common Beam Monitor Project [20].

⁹ $\sigma_{\text{coherent}} / (\sigma_{\text{incoherent}} + \sigma_{\text{coherent}}) = 0.0036 \approx 0$.

¹⁰ For the purpose of this thesis, quasi-parasitic is defined to mean that the beam is attenuated by less than 1%.

2 Calibrations at the Source-Testing Facility

2.1 Facility overview

The Source-Testing Facility (STF) is located in the Microbeam Hall of the Physics Department at Lund University and operated by the SONNIG Group of the Division of Nuclear Physics in collaboration with the ESS DG. It is a user facility which provides access to neutron and γ -ray sources. The facility also offers a variety of electronics components, detectors and data-acquisition systems (DAQ) to the user. Figure 2.1 shows an overview of the facility. Sources are stored in the interlocked area. Of particular use is a thermalizer which may be employed to reduce the energy of neutrons from radioactive sources to ~ 25 meV, the energy of interest for this project.

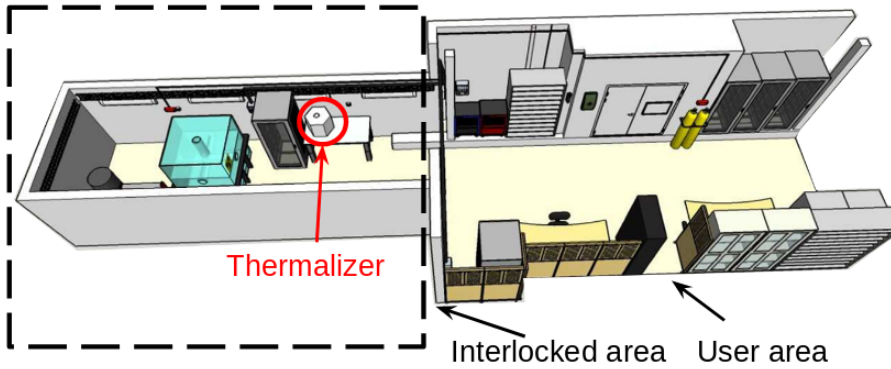


Figure 2.1. Overview of the Source-Testing Facility. Radioactive sources are stored in the interlocked area.

2.2 Apparatus

2.2.1 Radioactive sources

γ -ray

For all the measurements related to the neutron capture-based BM, ^{60}Co and ^{137}Cs sources were used. ^{60}Co is a dual-mode β^- emitter with a half-life $t_{1/2} = 5.27$ years. Figure 2.2(a) shows that the daughter product of the β^- emission are $^{60}\text{Ni}^*$ or $^{60}\text{Ni}^{**}$. Two characteristic γ -rays result from the de-excitation of the intermediate excited states of ^{60}Ni to the ground state. These characteristic γ -rays have energies 1.1732 MeV and 1.3325 MeV. ^{137}Cs is also a dual-mode β^- emitter with a half-life $t_{1/2} = 30.2$ years. Figure 2.2(b) shows that the daughter products of the β^- emission are $^{138}\text{Ba}^*$ or ^{138}Ba . One characteristic γ -ray results from the de-excitation of the intermediate excited state of ^{60}Ba to the ground state. This characteristic peak has energy 0.6617 MeV.

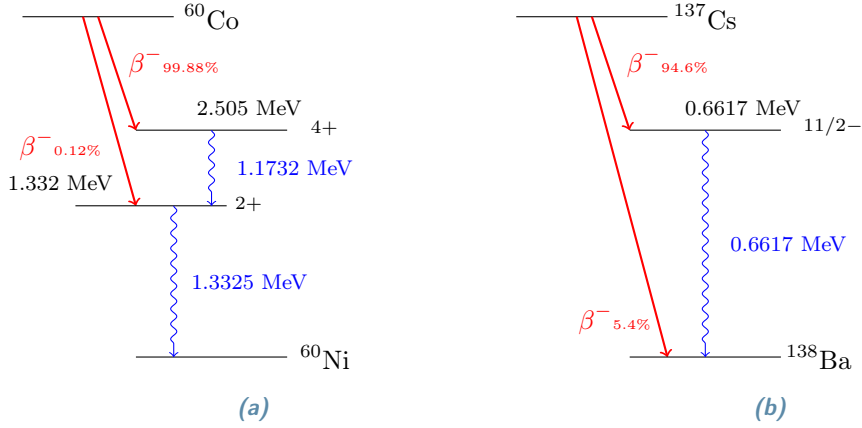


Figure 2.2. Decay schemes of the γ -ray sources. (a) ^{60}Co (b) ^{137}Cs .

Table 2.1 summarizes the characteristic γ -ray energies for the γ -ray sources.

Table 2.1. γ -ray sources and their characteristic energies.

Source	Energy [MeV]
^{60}Co	1.1732, 1.3325
^{137}Cs	0.6617

Neutron

The neutron source used in all the measurements related to the neutron scattering-based BM was an $^{241}\text{Am}/^9\text{Be}$ [21] source with activity $(1.106 \pm 0.015) \cdot 10^6$ n/s [22].¹¹ ^{241}Am is an α -emitter¹² with a half-life $t_{1/2}$ of 432.2 years. According to NuDat [22, 23], ^{241}Am decays via the emission of 25 different α -particles with a weighted-mean energy of 5.4768 MeV. For each of the α -emissions, there are many different decay modes. The daughter products of the α -emission can be an excited state of ^{237}Np . Figure 2.3 shows as an example the 0.060 MeV γ -ray released from the dominant decay branch.

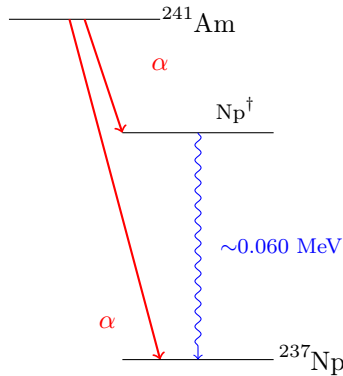
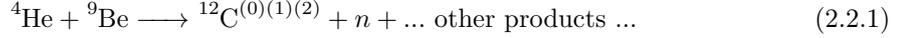


Figure 2.3. Simplified decay scheme of ^{241}Am . The dagger symbol represents the dominant excited state of ^{237}Np .

¹¹The $^{241}\text{Am}/^9\text{Be}$ neutron source calibration was performed at National Physical Laboratory, Teddington, Middlesex, UK, on 24 January 2012.

¹²An α -particle consists of two neutrons and two protons. It is the nucleus of the ^4He atom.

The α -particles then interact with ${}^9\text{Be}$, according to:



${}^{12}\text{C}$ may be created in its ground(0), first(1) or second(2) excited state. The ${}^{241}\text{Am}/{}^9\text{Be}$ source thus produces an additional characteristic 4.44 MeV γ -ray corresponding to the de-excitation of ${}^{12}\text{C}$ from the first excited state to the ground state.¹³

Simulations of the ${}^{241}\text{Am}/{}^9\text{Be}$ neutron source were essential to the results reported in this thesis. All of the simulations were performed using Geant4¹⁴ [24–26] together with the NCrystal package and the ESS simulation framework.¹⁵ The physics list used to replicate the source was QGSP_BIC_HP, while the physics list used for the simulation of the moderator and of the ${}^{\text{nat}}\text{V}$ was ESS_QGSP_BIC_HP_TS¹⁶. Finally the physics list used for the absorption of neutrons on ${}^{\text{nat}}\text{V}$ was LBE¹⁷. Figure 2.4 shows a simulated neutron spectrum compared to the neutron spectrum measured in Ref. [21]. The agreement is clearly excellent. This implementation of the ${}^{241}\text{Am}/{}^9\text{Be}$ source has thus been used for all the simulations performed in this thesis.

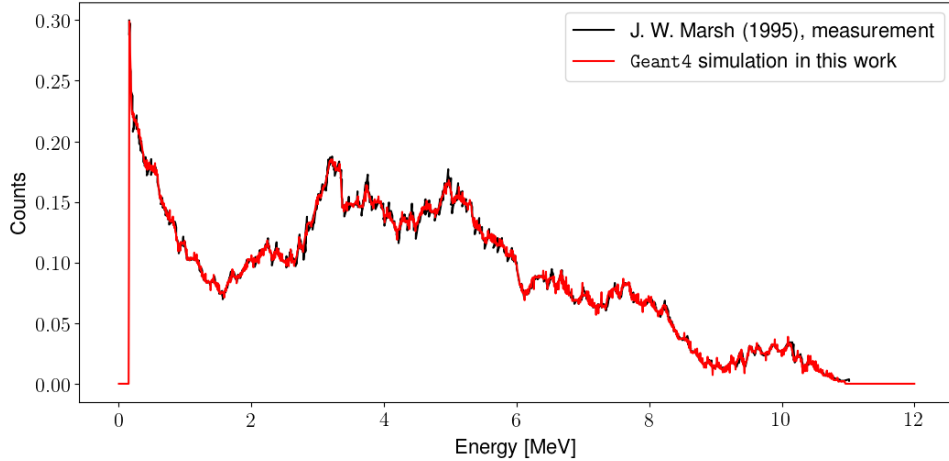


Figure 2.4. Geant4 ${}^{241}\text{Am}/{}^9\text{Be}$ neutron simulation. The simulation (red) is compared to the measurement from Marsh et al. [21] (black). Agreement is excellent.

2.2.2 Moderator

Moderation is the name for the physical process which slows down energetic neutrons. High-energy neutrons generally interact with matter via scattering. When an incident neutron with energy E scatters from a target, it transfers part of its energy according to:

$$E_R = \frac{4A}{(1+A)^2} (\cos^2 \theta) E, \quad (2.2.2)$$

where E_R is the kinetic energy of the recoiling nucleus, A is the mass of the target nucleus and θ is the scattering angle. Table 2.2 shows $(E_R/E)_{max}$ as a function of A . Clearly, the value of $(E_R/E)_{max}$ is highest for the lightest elements. As a consequence, hydrogen-rich materials are

¹³This γ -ray may be used to tag neutrons having energies lower than ~ 6 MeV.

¹⁴Geant4 (for GEometry ANd Tracking) is a Monte Carlo simulation platform for the passage of particles through matter. It was developed at Conseil Européen pour la Recherche Nucléaire (CERN).

¹⁵Geant4 treats elements as a dense gas. NCrystal and the ESS simulation framework are thus needed for realistic scattering simulations.

¹⁶This physics list was specifically developed for neutron scattering in crystal structures.

¹⁷LBE is one of the very few physics lists for which the activation of reaction products is allowed.

preferentially used for thermalizing energetic neutrons as ^1H is the most efficient material for moderation. A typical hydrogen-rich moderator is polyethylene $(\text{C}_2\text{H}_4)_n$.

Table 2.2. Maximum energy transfer as a function of A. Adapted from Ref. [27].

Target Nucleus	A	$(E_R/E)_{max}$
^1H	1	1.000
^2H	2	0.889
^3He	3	0.750
^4He	4	0.640
^{12}C	12	0.284
^{16}O	16	0.221

The relationship between the thickness of a moderator z and the number of thermalized neutrons I is given by:

$$\frac{I}{I_0} = e^{-\Sigma_{tot}z}, \quad (2.2.3)$$

where I_0 is the initial intensity of neutrons and Σ_{tot} is the macroscopic cross section for compound materials. This cross section is given by:

$$\Sigma_{tot} = \rho N_A (n_1 \sigma_1 + n_2 \sigma_2 + \dots) / M_m, \quad (2.2.4)$$

where ρ is the density of the compound, M_m is the molar mass, N_A is Avogadro's number, $\sigma_1, \sigma_2, \dots$ are the cross sections for elastic scattering for each of the elements within the compound and n_1, n_2, \dots are the corresponding numbers of atoms. The mean-free path $\lambda = 1/\Sigma_{tot}$ for polyethylene is $\lambda = 1.14$ cm. The number of collisions N required to reduce the energy of a neutron from E' to E'' is given by:

$$N = \frac{\ln(\frac{E'}{E''})}{\xi}, \quad (2.2.5)$$

where ξ is the average logarithmic energy decrement. ξ for a compound can be expressed as:

$$\xi = \frac{\sigma_1 \xi_1 + \sigma_2 \xi_2 + \dots}{\sigma_1 + \sigma_2 + \dots}, \quad (2.2.6)$$

where ξ_1, ξ_2, \dots are the average logarithmic decrements for each atom in the molecule of the compound. For polyethylene, $\xi = 0.902$ and the average number of collisions required to reduce the energy of 10 MeV neutrons to 25 meV is $N = 19.4$. Thus, ~ 20 cm of polyethylene is needed to thermalize a 10 MeV neutron. The moderating ratio $\xi \Sigma_{scattering} / \Sigma_{absorption}$ is the ratio of the macroscopic cross section for elastic scattering (desired) to the macroscopic cross section for absorption (undesired). The polyethylene thermalizer used in this work was designed based upon optimizing the moderating ratio and employs ~ 7.5 cm of polyethylene.

Figure 2.5 shows the thermalizer. In the middle of the polyethylene block there is a hole for the radioactive source. The polyethylene block is housed in an ^{nat}Al container covered with borated¹⁸ paint. The ^{nat}Al housing has a small back-side opening and a larger front-side opening. This thermalizer was used as a moderator for all the calibrations performed at the STF.

¹⁸¹⁰B has an absorption cross section of 3850 b for 1.8 Å neutrons [23]. The paint is used to absorb moderated neutrons escaping from the moderator in all directions save the small back-side opening and larger front-side opening in order to define moderated neutron beams.

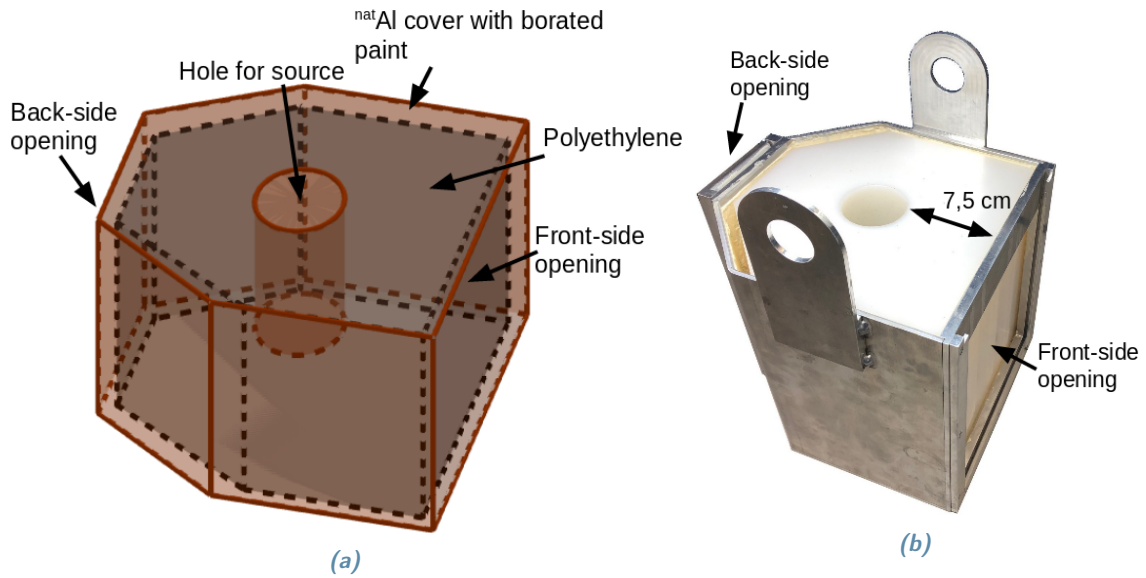


Figure 2.5. The neutron thermalizer. It consists of a block of polyethylene with a hole for a neutron source. The block of polyethylene is housed in an ^{nat}Al container coated with borated paint. (a) Sketch (b) Photograph.

Figure 2.6 shows simulations of the neutron-energy distributions associated with the $^{241}\text{Am}/^9\text{Be}$ source both before and after thermalization. The simulations predict that 45% of the neutrons radiated by the source will be captured by the polyethylene. Figure 2.6 shows the energy distribution of neutrons after thermalization. The inset shows that 3.7% of the neutrons exiting the polyethylene block are in the thermal-energy region. The total efficiency of the thermalizer is thus 1.7%. After correction for solid angle, a thermal-neutron flux of 26 n/s/cm^2 for each of the openings is anticipated.

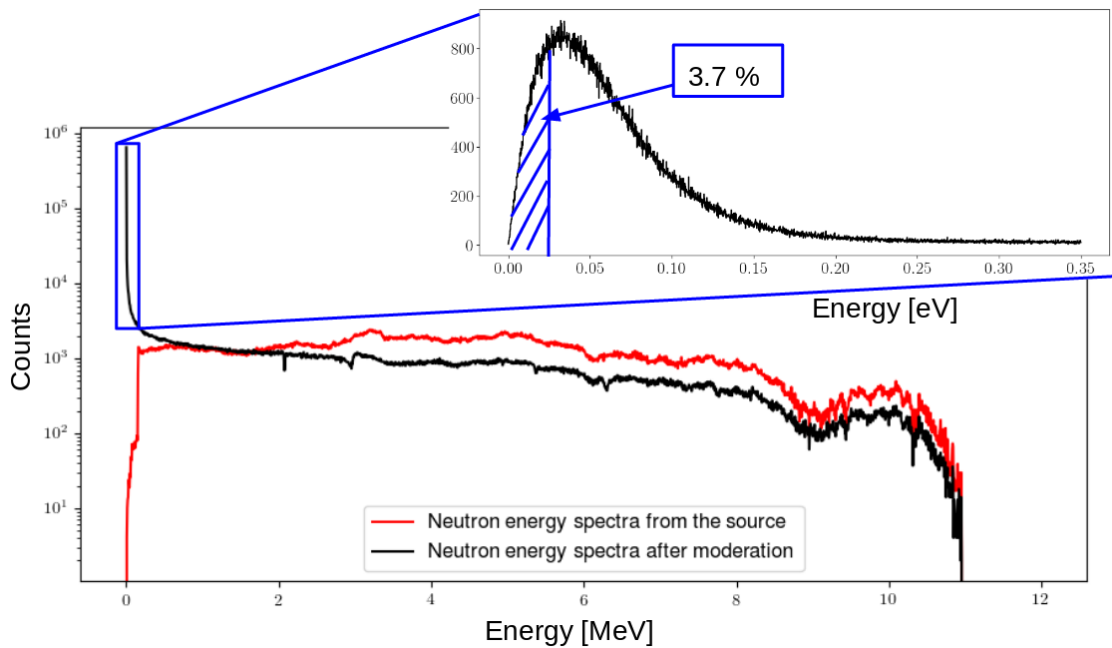


Figure 2.6. $^{241}\text{Am}/^9\text{Be}$ neutron simulations before and after thermalization. The inset shows the fraction of the neutrons which have been thermalized.

2.2.3 Vanadium foils

^{nat}V is a transition metal. It has a high melting point (2183 K) and high boiling point (3680 K). ^{nat}V almost never occurs naturally as a pure metal, but rather as part of a compound. Very importantly, ^{nat}V is the only element in the periodic table other than hydrogen that scatters neutrons isotropically [9–13]. This means that the crystal structure of ^{nat}V does not allow the scattered neutron waveforms to interfere with one another.¹⁹ Table 2.3 shows some fundamental properties of ^{nat}V .

Table 2.3. Fundamental properties of ^{nat}V .

Property	Value
Melting point	2183 K
Boiling point	3680 K
Density	6.0 g cm ⁻³
Relative atomic mass	50.942 amu
Electron configuration	[Ar] 3d ³ 4s ²
Atomic number	23
Common isotopes	⁵⁰ V, ⁵¹ V

The ^{nat}V used for this prototype was purchased from Goodfellow [17]. It is a mixture of ⁵¹V (99.75%) and ⁵⁰V (0.25%) and other materials such as ^{nat}Ag , ^{nat}Al and ^{nat}Si . For the initial characterization of the BM at the STF, 7 pieces of ^{nat}V (6 thick foils and 1 rod) were investigated, see Fig. 2.7 and Table 2.4. For all the STF calibrations, only the foils with thicknesses 3.15 mm and 1 mm were used.²⁰

Table 2.4. ^{nat}V foil dimensions and calculated attenuations.

Type	Length [mm] $\pm 20\mu\text{s}$			Attenuation [%]	
	a	b	z	1.8 Å	3.35 Å
Foil	50	50	3.15	10.1	28.0
Foil	50	50	1.00	3.5	9.9
Foil	50	50	0.20	0.70	2.1
Foil	50	50	0.125	0.5	1.1
Foil	50	50	0.04	0.1	0.4
Foil	50	50	0.02	0.1	0.2
Rod	50	-	12.5	41.7	92.6

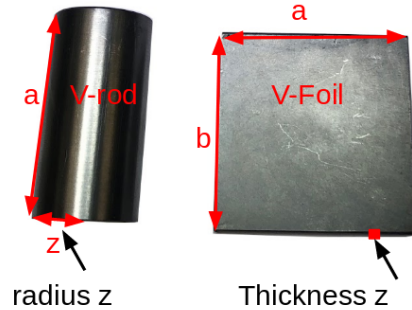


Figure 2.7. Photograph of ^{nat}V rod and foils.

2.2.4 Detectors

γ -ray

The γ -ray detectors used in this thesis are scintillation detectors. Scintillation involves the incident γ -ray exciting the electrons in a scintillation material. As these electrons de-excite, they emit visible light. Basic properties of scintillation materials are:

- Density and atomic number. Higher density and higher atomic number are desirable for detecting higher energy γ -rays.

¹⁹Due to the fact that ^{nat}V isotropically scatters neutrons, it is often added to other metals to dampen crystal-vibrational modes and strengthen the resulting alloy.

²⁰The pieces tested at the STF are rather thick compared to the 125 μm foil that is suggested for use in an actual beam of thermal neutrons. For the flux of neutrons incident on the detectors to be observed, it was necessary to combine the thickest foils.

- Light output. The amount of light emitted per unit of incident energy is a function of the material. Unfortunately, this is not always constant, making the output of some scintillators non-linear.
- Decay time. The shorter the duration of the light pulse, the easier it is to distinguish between an initial and subsequent pulses.
- Mechanical and optical properties. Hygroscopic²¹ scintillators may only be used in sealed containers to prevent degradation.

The scintillation crystals used for these measurements were CeBr_3 and $\text{LaBr}_3:\text{Ce}$, see Table 2.5.

Table 2.5. Scintillation properties of $\text{LaBr}_3:\text{Ce}$ and CeBr_3 crystals. Adapted from [28].

Material	Material Density ρ [g/cm ³]	Emission Maximum λ_{max} [nm]	Decay Constant ²² t_γ [ns]	Refractive Index n	Conversion Efficiency ²³	Hygroscopic
CeBr_3	5.23	370	18 ns	1.9	130	yes
$\text{LaBr}_3:\text{Ce}$	4.9	380	35	1.9	140	yes

Once the γ -ray is converted to scintillation light, a photomultiplier tube (PMT) is used to convert this scintillation light to an electrical signal. A PMT consists of a photocathode that converts scintillation photons to photoelectrons and dynodes that amplify the photoelectrons into a larger pulse of electrons. The resulting signal consists of a current pulse that is proportional to the scintillation light. Figure 2.8 shows the scintillation crystal connected to the PMT which is in turn connected to a base. The base has connections for High Voltage (HV) and the signal.

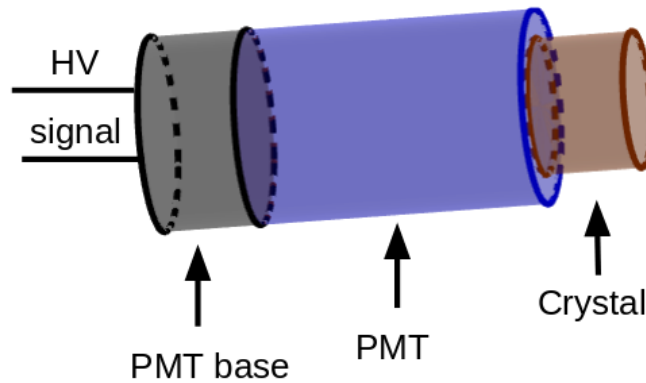


Figure 2.8. Schematic overview of a scintillation detector. A scintillation crystal (brown) is connected to the PMT (blue) and subsequently to the PMT base (grey).

This pulse is passed to a preamplifier or amplifier depending on the data-acquisition system (DAQ) system. Figure 2.9 shows photographs of the scintillation detectors. The PMTs used for both scintillators were cylindrical with 1.55” diameters.

²¹Hygroscopic materials attract water molecules from the surrounding environment at room temperature and retain them.

²²Effective average decay time for γ -rays

²³Relative scintillation signal at room temperature for γ -rays when coupled to a photomultiplier tube

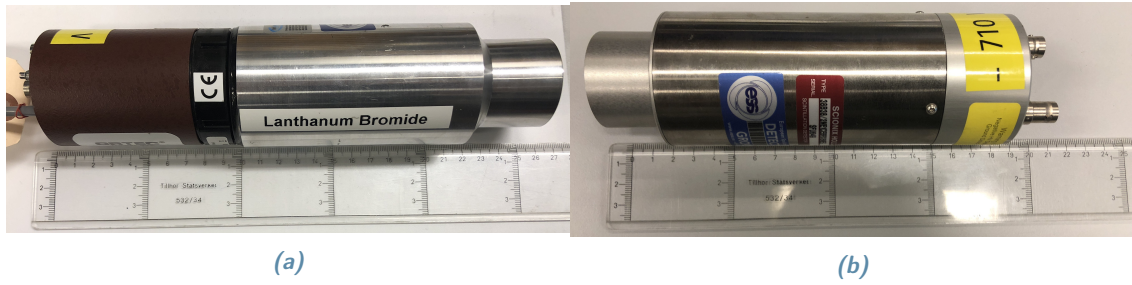


Figure 2.9. Photographs of the $\text{LaBr}_3\text{:Ce}$ and CeBr_3 detectors. (a) $\text{LaBr}_3\text{:Ce}$ detector (together with preamplifier) (b) CeBr_3 detector.

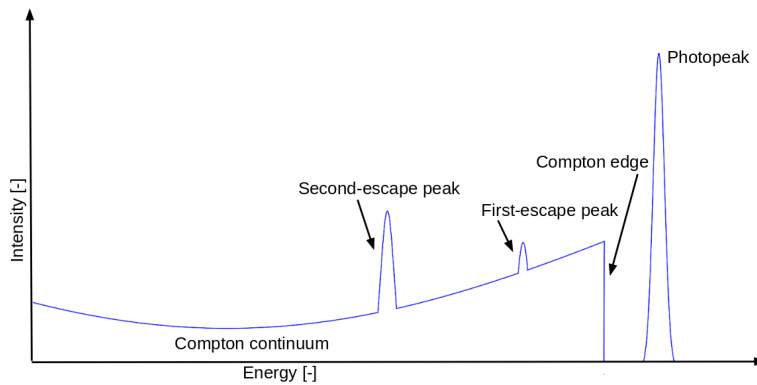


Figure 2.10. Response of a scintillation detector to a monoenergetic γ -rays.

Figure 2.10 shows the ideal response of a smaller scintillation detector to monoenergetic γ -rays. The first- and second-escape peaks may occur when the γ -ray has energy larger than 1.022 MeV. This energy corresponds to the spontaneous creation of a positron-electron pair. The stopped positron can then annihilate with another electron to produce a pair of 0.511 MeV γ -rays. If one of these γ -rays escapes the scintillator without detection, the first-escape peak results. If both of these γ -rays escape the scintillator without the detection, the second-escape peak results. The Compton edge and continuum correspond to γ -rays undergoing single or multiple scattering respectively. The kinetic energy T_e of a recoiling electron corresponding to a single Compton event is given by [29]:

$$T_e = \frac{E_\gamma^2(1 - \cos \theta)}{m_e c^2 + E_\gamma(1 - \cos \theta)}, \quad (2.2.7)$$

where θ is the scattering angle between the γ -ray and the electron corresponding to the Compton edge. At $\theta = \pi$:

$$T_e = \frac{2E_\gamma^2}{m_e c^2 + 2E_\gamma}, \quad (2.2.8)$$

corresponding to the maximum electron energy.

The detector resolution R is given by:

$$R = \frac{\Delta E_{\text{FWHM}}}{E}, \quad (2.2.9)$$

where E is the mean of the Gaussian distribution fitted on the γ -ray peak and ΔE_{FWHM} is the full-width-at-half-maximum (FWHM) of this distribution. It is a physical quantity that characterizes the response of the detector to monoenergetic incident γ -rays. When a large number of monoenergetic events are converted to charge by a detector, resolution effects spread charges randomly according to a Gaussian distribution. R may be characterized by the ratio of the FWHM

of the Gaussian peak to the energy of the monoenergetic γ -rays. Figure 2.11 shows the “smearing” effect of resolution. Note that this discussion of the energy resolution may be generalized to any type of incident radiation by substituting “particle” for “ γ -ray”.

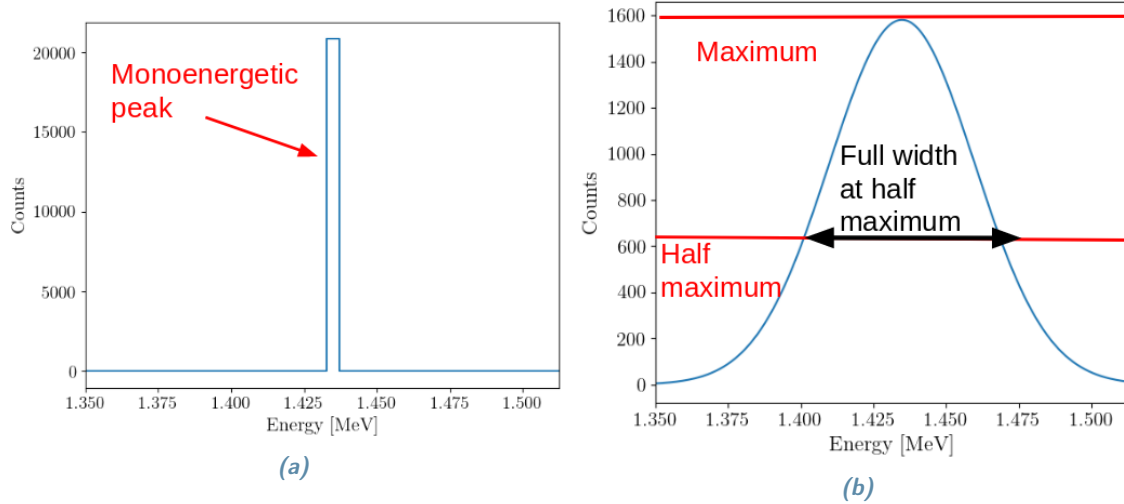


Figure 2.11. An illustration of energy resolution. (a) The incident monoenergetic beam, limited only by the binning of the histogram. (b) “Smearing” of the detected beam due to the detector energy resolution of 4%.

Thermal Neutron

The detection of thermal neutrons using a ^3He detector relies on the relatively high probability for thermal neutrons to react with ^3He , $\sigma = 5330 \text{ b}$ at 1.8 \AA [30]. The reaction is given by:



The Q -value is shared by the reaction products in inverse proportion to their mass, so that ^3H recoils with 191 keV while the proton recoils with 573 keV. Figure 2.12 shows a typical spectrum produced when a ^3He tube is exposed to thermal neutrons. The full-deposition peak corresponds to both the proton and the ^3H depositing all of their kinetic energy in the gas. The “wall” effect corresponds to when only the energy of proton is fully deposited in the gas as the ^3H collides with the detector wall or when only the energy of the ^3H is fully deposited in the gas as the proton collides with the detector wall. The smaller the detector, the bigger the wall effect.

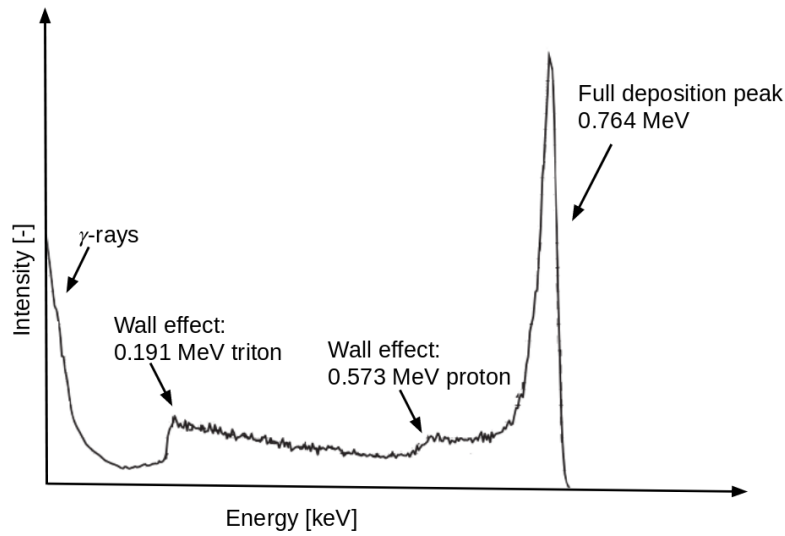


Figure 2.12. Response of a ^3He detector to thermal neutrons. γ -rays are deposited in the low energy region to the far left, while the ^3H and proton wall effects appear at 0.191 MeV and 0.573 MeV respectively. The full-deposition peak is shown at 0.764 MeV. Adapted from Ref. [31].

Figure 2.13 shows a conceptual design of a ^3He detector. The ^3He gas is stored in the steel container which also acts as a cathode. A thin anode wire is located in the middle of the tube. When HV is applied, the anode wire collects the secondary ions produced by the proton and ^3H as they ionize the gas resulting in a pulse proportional to the energy deposited in the gas.

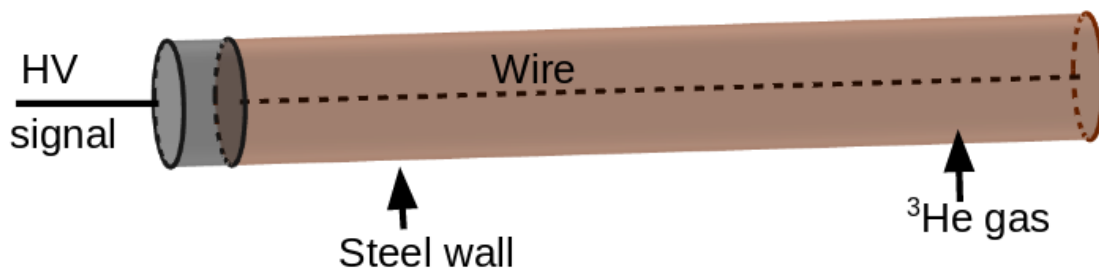


Figure 2.13. Schematic overview of a ^3He detector. The signal wire (black dotted line) is placed in sealed volume of ^3He gas (brown area) and connected to a base (black). HV is applied and the signal extracted via this base.

Figure 2.14 shows a photograph of one of the four ^3He proportional counters used in this work. All of the ^3He counters were purchased from Reuter-Stokes [32] and were $1'' \times 3.94''$ with a pressure of 8 bar.

2.2.5 Data-acquisition system

CeBr₃

Figure 2.15 shows the DAQ system for the CeBr₃ detector. Operated at -710 V , the detector produced a negative polarity current pulse that was passed to a Nuclear Instrumentation Module (NIM) ORTEC 673 amplifier/shaper [33]. This module amplified and inverted the pulse. A Rhode & Schwartz [34] oscilloscope was used to visually monitor the pulses periodically. The pulses were passed to a MCA 8000D pocket MCA [35]. The MCA integrated the pulses to yield the charge



Figure 2.14. Photograph of the ^3He detector. From left: the yellow lid protects the high-voltage/signal connector. The dark grey cylinder holds the ^3He gas.

corresponding to each scintillation event and binned these charges resulting in histograms that were stored for subsequent offline analysis.

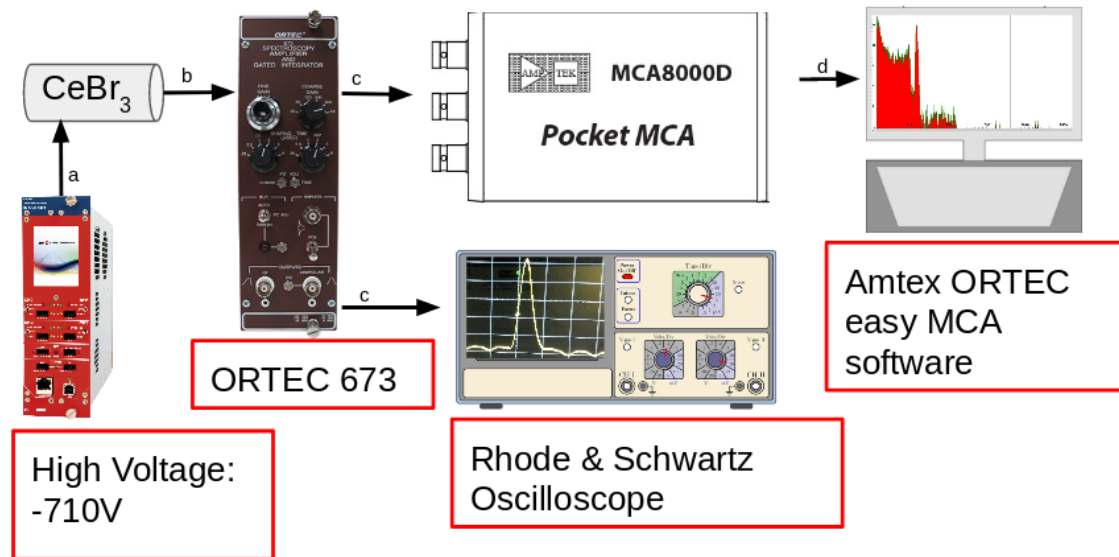


Figure 2.15. Data-acquisition system for the CeBr_3 detector. a - HV cable, b - LEMO cable, negative polarity current pulse, c - LEMO cable, positive polarity current pulse, d - MCA-USB link. From left: The HV power supply is connected directly to the base of the detector. The anode current pulse is then amplified, shaped, inverted and passed to the MCA. The DAQ software histograms and displays the resulting spectra.

LaBr₃:Ce and ^3He tube

Figure 2.16 shows the DAQ system for the ^3He and LaBr₃:Ce detector. New to the circuit is the preamplifier. Operated at +1275 for the ^3He detector and +600 V for the LaBr₃:Ce detector, each detector produced a positive current pulse that was passed to an ORTEC 142PC [36] for the ^3He detector and ORTEC 276 preamplifier [37] for LaBr₃:Ce detector. From the preamplifier, the current pulse was passed to a NIM ORTEC 673 amplifier/shaper [33]. A Rhode & Schwartz [34] oscilloscope was used to visually monitor the pulses periodically. The pulses were passed to a MCA 8000D pocket MCA [35]. The MCA integrated the pulses to yield the charge corresponding to each event and binned these charges resulting in histograms that were stored for subsequent offline analysis.

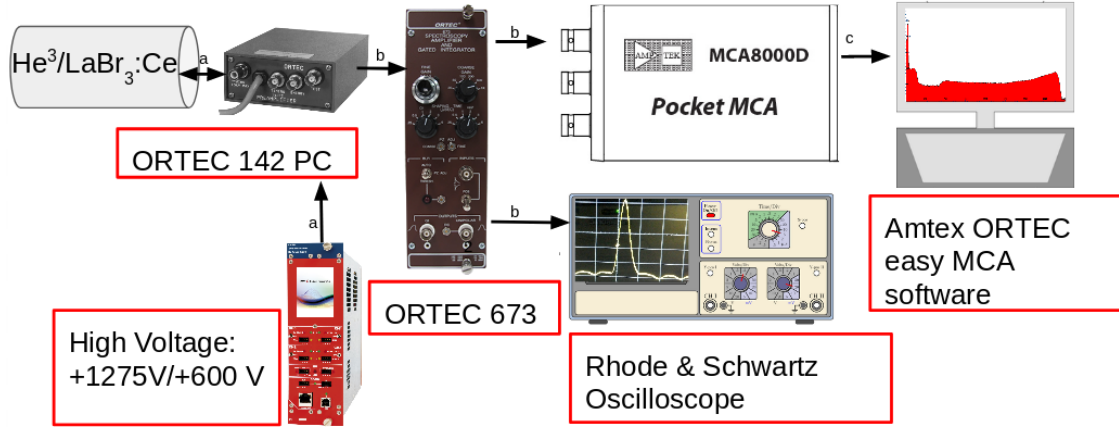


Figure 2.16. Data-acquisition system for the Helium and $\text{LaBr}_3:\text{Ce}$ detectors. *a* - HV cable, *b* - LEMO cable, positive polarity current pulse, *c* - MCA-USB link. From left: the HV power supply is connected to preamplifier which is connected to the base of the detector. The current pulse from the preamplifier is then amplified and shaped and passed to the MCA. The DAQ software histograms and displays the resulting spectra.

Table 2.6 presents a summary of the settings used for the electronics for each of the detectors.

Table 2.6. Overview of the data-acquisition systems.

Detector	$\text{LaBr}_3:\text{Ce}$, Fig. 2.9a	CeBr_3 , Fig. 2.9b	^3He , Fig. 2.14
Crystal dimensions	1.5"x 1.5"	1.5"x 1.5"	1"x 3.94"
HV	+600 V	-710 V	+1275 V
Preamplifier	ORTEC 276	No preamp	ORTEC 142PC
Amplifier	ORTEC 673	ORTEC 673	ORTEC 673
			TENNELEC TC 244
Amplifier (gain)	20	20	varied
Amplifier (fine gain)	70	70	0
Shaping time	0.25 μs	0.5 μs	varied ²⁴
Input	Positive	Inverted	Positive
Self Calibrating Peak	No	1.45 MeV ²⁵	(0.764, 0.191 0.573) MeV

2.3 Measurements and analysis

2.3.1 Absorption

Activation

Measuring γ -ray spectra from neutron-activated $^{\text{nat}}\text{V}$ when the neutron source is present in the experimental setup is very challenging. The $^{\text{nat}}\text{V}$ sample was thus activated by placing it next to the source of thermalized neutrons and then moving it to a source-free environment where the de-excitation γ -ray spectra were measured. The maximum number of particles activated in the $^{\text{nat}}\text{V}$ sample N is given by:

$$N = \frac{\Phi_0(1 - e^{-n\sigma z})}{\lambda}(1 - e^{-\lambda t}), \quad (2.3.11)$$

²⁴While the shaping constants for the scintillation detectors were fixed, for the ^3He detector the shaping constant was varied. The best energy-resolution spectra were observed at 12 μs , but this was not optimal. See Appendix A.1.

²⁵ $e^- + ^{138}\text{La} \xrightarrow{\text{electron capture}} ^{138}\text{Ba}^* \longrightarrow ^{138}\text{Ba} + \gamma (1.45\text{MeV}).$

where Φ_0 is the initial flux, n is the number density, σ is the absorption cross section, z is the thickness, λ is the decay constant and t is the time of irradiation, see the Table 2.7. Figure 2.17 shows the total number of activated ^{nat}V atoms N as a function of irradiation time t . Saturation clearly occurs at about 30 min.

Table 2.7. Parameters for ^{nat}V activation calculations.

Quantity	^{nat}V foils (1 mm + 3.15 mm)	^{nat}V rod
Initial flux Φ_0 [n/s]	7900	3950
Number density n [cm^{-3}]	$7.09 \cdot 10^{22}$	$7.09 \cdot 10^{22}$
Cross section for absorption σ [cm^{-2}]	$5.08 \cdot 10^{-24}$	$5.08 \cdot 10^{-24}$
Thickness z [cm]	0.415	1.25
Decay constant λ [s^{-1}]	0.0032	0.0032

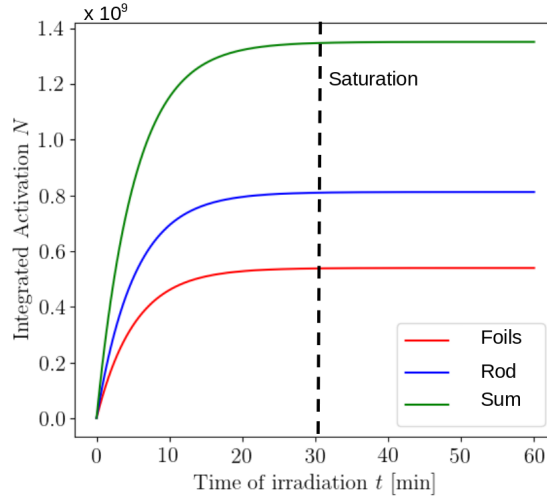


Figure 2.17. Activation of the ^{nat}V samples as a function of time.

Figure 2.18 shows the experimental setup for the activation of ^{nat}V . The 3.15 mm and 1 mm foils were used as a single activation target. The rod was also irradiated. These targets were placed in front of the large thermalizer opening. Water jugs and additional shielding were used to increase the number of thermalized source-related neutrons. For most of the measurements, the irradiation time was actually much longer, see Table 2.8.

Table 2.8. $^{nat}\text{V}^*$ de-excitation data sets.

LaBr ₃ :Ce run no.	$T_{\text{activation}}$ [h]	$T_{\text{measurement}}$ [min]			CeBr ₃ run no.	$T_{\text{activation}}$ [h]	$T_{\text{measurement}}$ [min]		
		T_{Fg}	T_{Bg}	T_{cal}			T_{Fg}	T_{Bg}	T_{cal}
1	23	10	-	-	1	12	28	50	10
2	2	100	50	-	2	2	25	100	10
3	24	100	50	-	3	2	25	70	10
4	2	20	20	20	4	2	28	50	10
5	2	20	50	20					
6	12	20	10	5					
7	2	20	180	5					
8	2	20	100	5					
9	2	20	100	10					
10	2	20	10	10					

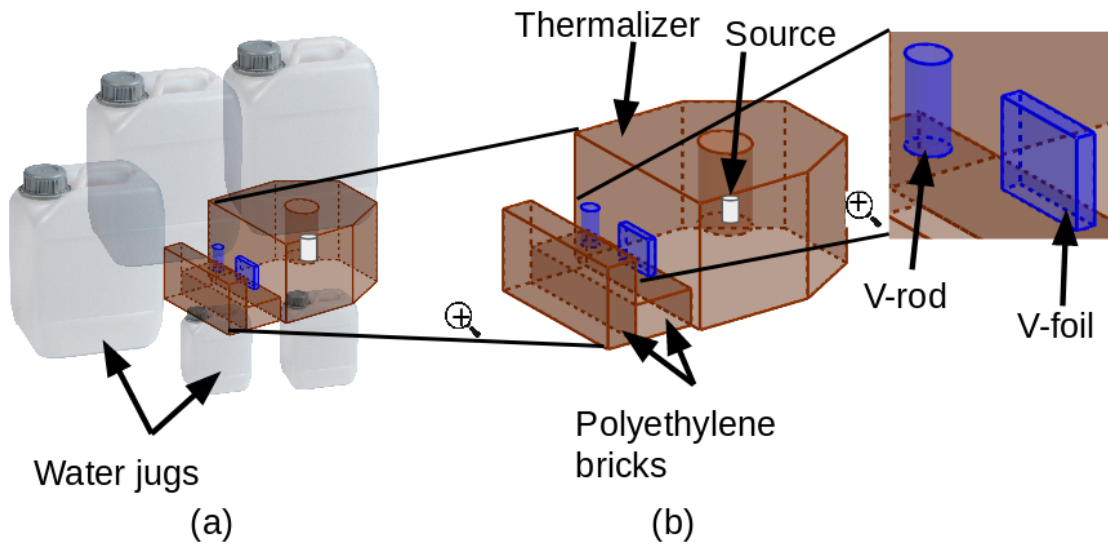


Figure 2.18. Setup for the activation of ^{nat}V . (a) Overview including shielding. (b) The inset shows the ^{nat}V rod and foils positioned in front of the large thermalizer opening.

De-excitation

The activated ^{nat}V samples were quickly (~ 20 s) moved to a source-free environment. Figure 2.19 shows the samples placed directly in front of the γ -ray detector to maximize its acceptance. Figure 2.19(c) shows the thick lead castle that was used to shield the detector from room background.

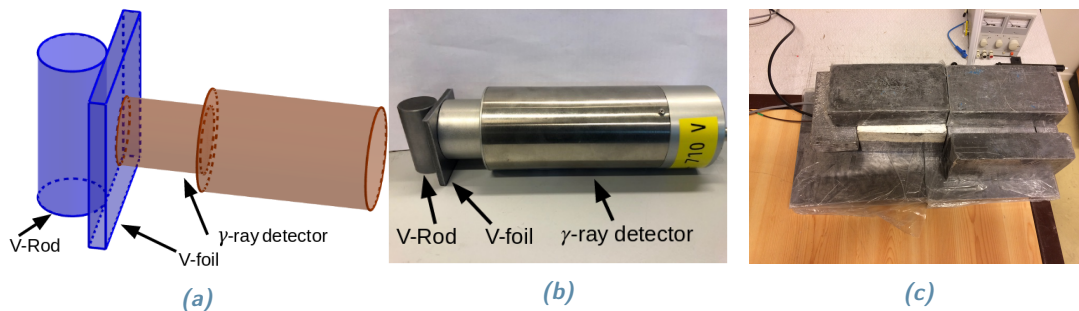


Figure 2.19. Setup for the activated ^{nat}V de-excitation γ -ray measurements. (a) Sketch. (b) Photograph of the detector. (c) Photograph of the detector inside the lead castle.

For each measurement, many datafiles were obtained. These files were stored in increments of 30 s for foreground (Fg) runs and every 5 minutes for background (Bg) runs to enable a time-dependent analysis of the data. For the total length of each measurement see Table 2.8.

Figure 2.20 shows the data-analysis sequence for the de-excitation γ -ray measurements. The goal was to produce calibrated γ -ray energy spectra. The Bg data were normalized with respect to time. The Fg data were corrected using the time-normalized background data. The resulting spectrum was then calibrated for energy and cross checked using Geant4 simulations.

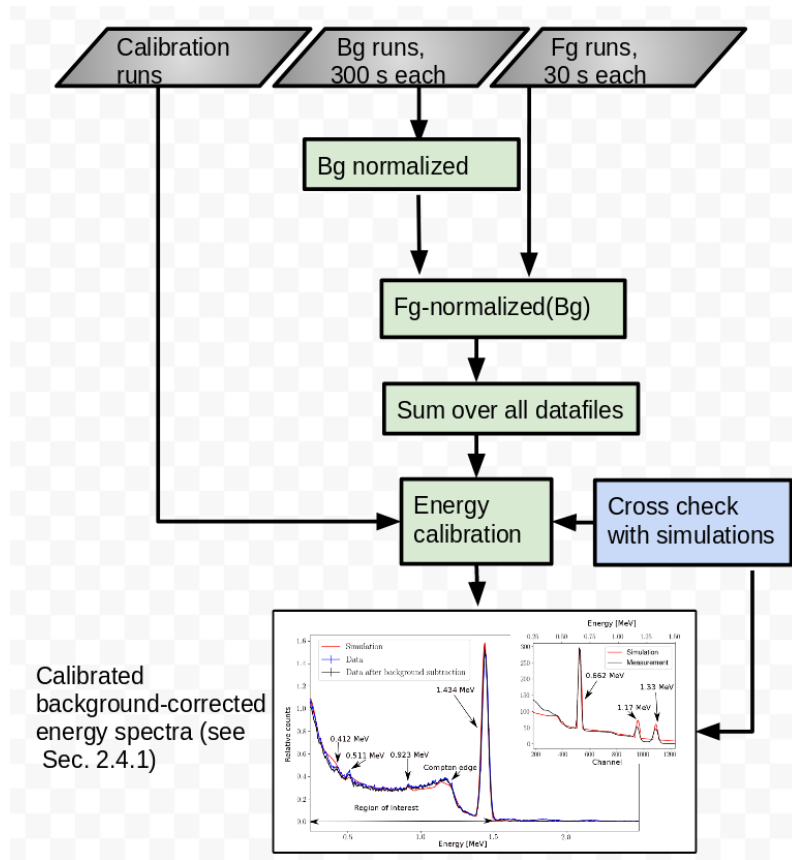


Figure 2.20. The de-excitation γ -ray analysis. The grey diamonds represent input, the green boxes represent processing and the blue box represents the cross check. The resulting spectrum is shown as a thumbnail and discussed in detail in Sec. 2.4.1.

Figure 2.21 shows the data-analysis sequence for the cross check performed on the results from the absorption measurements. A region-of-interest (RoI) containing the 1.434 MeV γ -ray corresponding to the decay of $^{52}\text{Cr}^*$ was integrated and its time evolution investigated in bins of 30 s. The goal was to determine the β^- decay constant for $^{52}\text{V}^*$ as a check of the behavior of the γ -rays corresponding to this peak associated with the de-excitation of $^{52}\text{Cr}^*$, and in doing so, prove the 1.434 MeV peak was of interest.

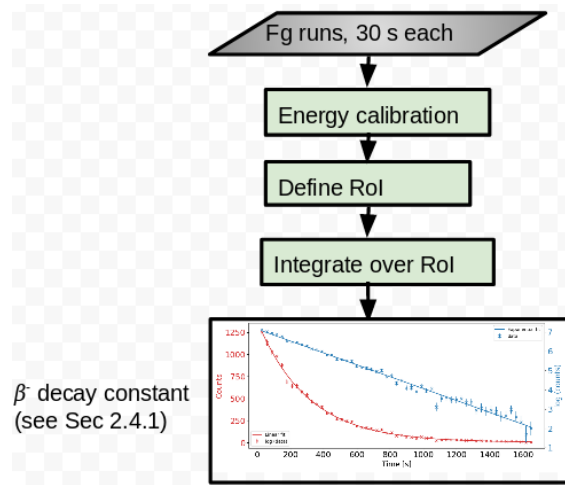


Figure 2.21. The de-excitation γ -ray analysis cross check. The grey diamonds represent input and the green boxes represent processing. The resulting spectrum shown as a thumbnail is discussed in detail in Sec. 2.4.1.

2.3.2 Scattering

Measuring scattered-neutron spectra from ^{nat}V when the neutron source is present in the experimental setup is also very challenging. Therefore, a boron-coated sleeve was employed to shield the ^3He detector from thermal neutrons incident upon all sides of the detector save for a very small sleeve opening which was parallel to the symmetry axis of the gas tube. Figure 2.22 shows the ^{nat}V samples placed in front of the sleeve opening close to the small thermalizer opening. Data were recorded both with and without the ^{nat}V present. The goal of the measurements was to identify the increase in detected thermal-neutron rate when the ^{nat}V was present. As this increase was very small, additional measurements were performed to ensure reproducibility. These additional measurements involved systematic changes to the geometry of the setup which included:

- placing the borated sleeve to the left and to the right side of the thermalizer,
- rotating the thermalizer,
- measuring the response using the large thermalizer opening.

The complete set of measurements are shown in Table 2.9.

Table 2.9. Neutron-scattering measurements on the ^{nat}V foils.

Run	Borated sleeve	Position of the sleeve	^{nat}V	Opening	Duration [min]
1	No	Middle	No	Small	240
2	Yes	Middle	No	Small	150
3	Yes	Right, 135°	No	Small	600
4	Yes	Left, 90°	Yes	Small	250
5	Yes	Right, 90°	No	Small	270
6	Yes	Right, 90°	Yes	Small	560
7	Yes	Left, 90°	No	Small	310
8	Yes	Left, 90°	Yes	Small	600
9	Yes	Left, 90°	No	Large	600
10	Yes	Left, 90°	Yes	Large	1200
11	Yes	Right, 90°	No	Large	600
12	Yes	Right 90°	No	Large	280
13	Yes	Right 90°	Yes	Large	80
14	No	Middle	No	Bare Source	840
15	Yes	Middle	No	Bare Source	170
16	Yes	Middle	No	Bare Source	930
17	No	Middle	No	Large	230
18	No	Middle	No	Large	940

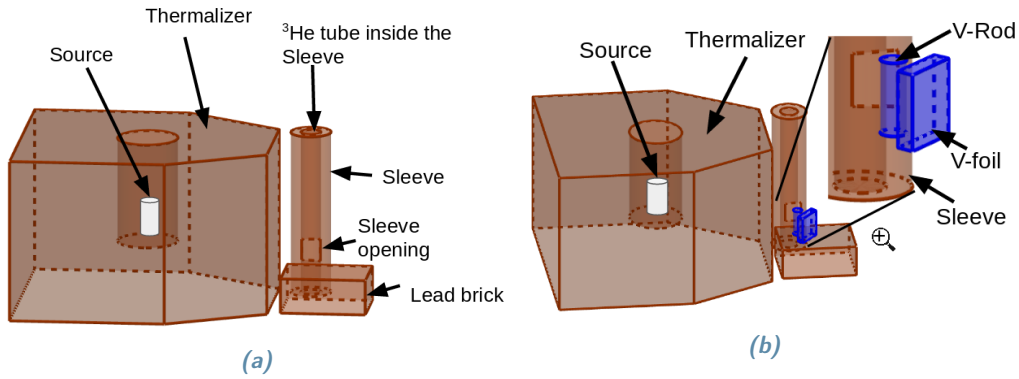


Figure 2.22. Setup for the ^{nat}V neutron-scattering measurements. The $^{241}\text{Am}/^9\text{Be}$ source (white) is shown in the thermalizer. (a) No ^{nat}V configuration (b) ^{nat}V (blue) in position configuration.

Figure 2.23 shows the data-analysis sequence for the neutron-scattering measurements. The Bg and Fg data were energy calibrated, gain matched, summed over all datafiles, time normalized and subtracted from each other. The resulting spectrum is discussed in detail in Sec. 2.4.2.

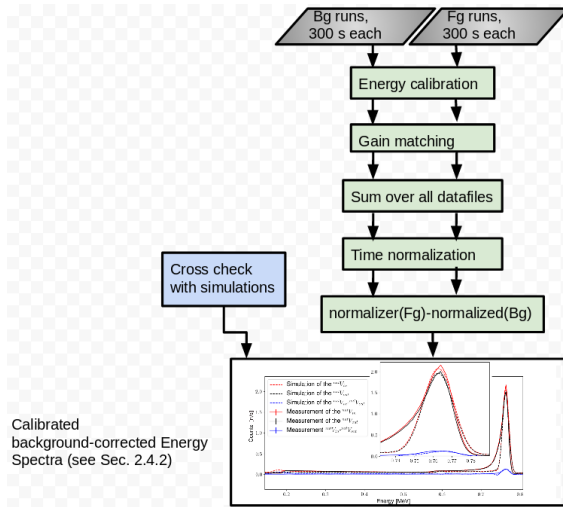


Figure 2.23. The neutron-scattering analysis. The grey diamonds represent input, the green boxes represent processing and the blue box represents the cross check. The resulting spectrum shown as a thumbnail is discussed in detail in Sec. 2.4.2.

2.4 Results

2.4.1 Absorption

Figure 2.24 shows the background-corrected γ -ray spectrum from the de-excitation of $^{52}\text{Cr}^*$ subsequent to the β^- decay of $^{52}\text{V}^*$ measured using the CeBr_3 detector. The inset shows the result of the calibration measurements performed using ^{60}Co and ^{137}Cs sources. Both spectra are compared to the **Geant4** simulation. In the inset the three characteristic source-related γ -ray peaks (0.662 MeV, 1.173 MeV and 1.333 MeV) are clearly visible. A 4.5% smearing was phenomenologically applied to the result of the **Geant4** simulation to account for detector resolution. The normalization was fixed by matching the integrals of the 0.662 MeV peak in ^{137}Cs . The main panel of Fig. 2.24 shows the background-corrected γ -ray spectrum. The 1.434 MeV γ -ray from the de-excitation of $^{52}\text{Cr}^*$ is clearly visible. The corresponding Compton edge at ~ 1.25 MeV may also be seen and hints of the first-escape peak at 0.930 MeV and second-escape peak at 0.412 MeV are also present. Furthermore, there may be a peak at 0.511 MeV which could originate from the recombination of a positron-electron pair. As in the inset, a 4.5% smearing was phenomenologically applied to the result of the **Geant4** simulation to account for the resolution of the detector. The normalization was fixed by matching the integrals of the 1.434 MeV peak.²⁶ The simulation matches the behavior of the data very well.

Figure 2.25 shows the time evolution of the background-corrected data integrated over $0 < \text{RoI} < 1.5$ MeV. The time constant of the decay was extracted from both a linear fit and a logarithmic fit of the radioactive decay law to these data which were binned in 30 s intervals. The statistically weighted fits to the data agree excellently.

²⁶Since thermalization in the polyethylene and de-excitation in $^{\text{nat}}\text{V}$ required different physics lists, the post-thermalizer neutron source-related simulation results were used as a generator for the de-excitation simulations. The resulting phase space was filtered for events which originated with neutron capture in the $^{\text{nat}}\text{V}$ foil.

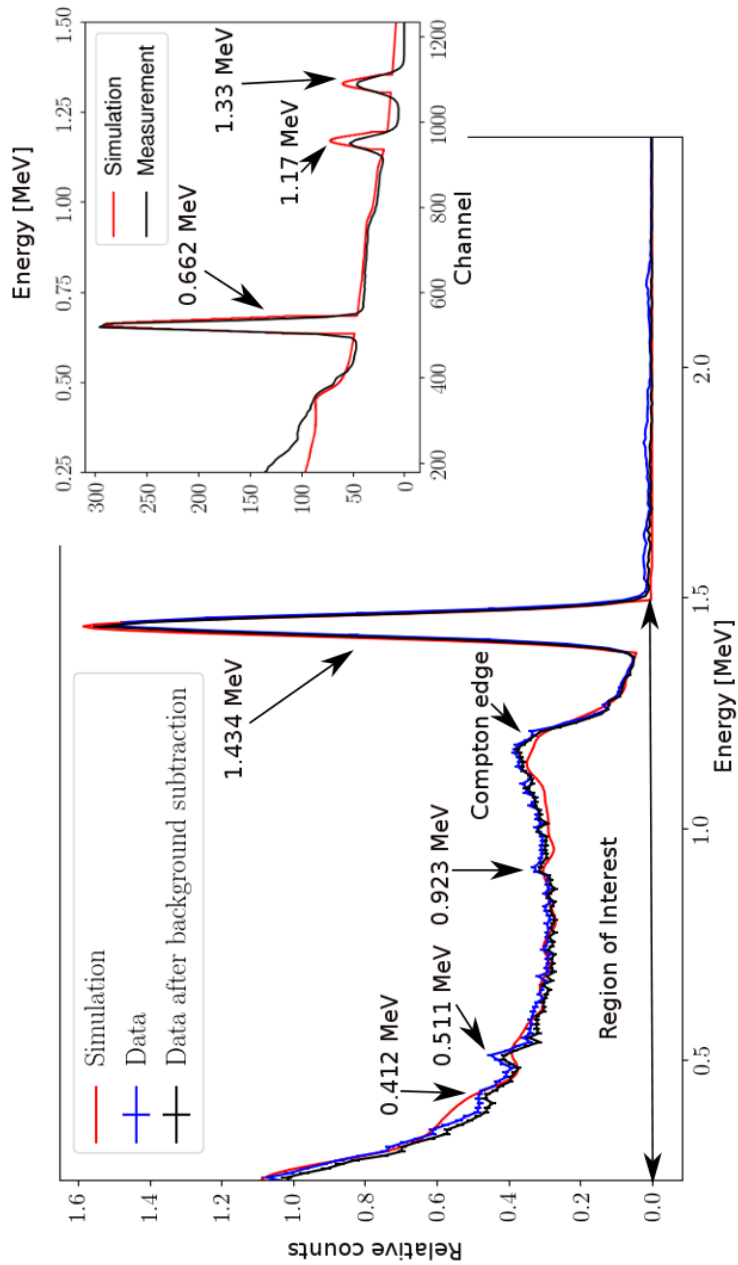


Figure 2.24. γ -ray spectra from activated ^{nat}V . The inset shows calibration data together with the Geant4 simulation. The characteristic peak at 1.434 MeV corresponding to the de-excitation of $^{52}\text{Cr}^*$ is clearly evident. In both cases, the simulated curves reproduce the data very well.

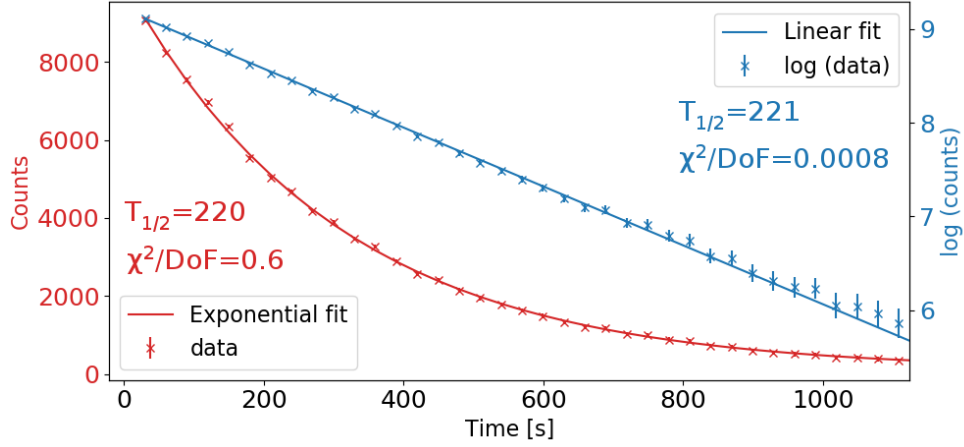


Figure 2.25. Time constant of the activated ^{nat}V decay. Both the linear and logarithmic investigation are shown.

Table 2.10 summarizes the results. They are very consistent and clearly demonstrate that, as both the energy and the decay constant are as anticipated, the investigated peak corresponds to neutron capture on ^{nat}V .

Table 2.10. The decay constant for the de-excitation of $^{nat}\text{Cr}^*$. The actual decay constant is $\lambda = 0.00308$, corresponding to $T_{1/2} = 225$ s. The data were consistent for both detectors and both methods.

Detector	Decay constant λ [s ⁻¹]	Half-life $T_{1/2}$ [s]
LaBr ₃ :Ce	0.0032 ± 0.0006	217 ± 5
CeBr ₃	0.0031 ± 0.0002	223 ± 2

2.4.2 Scattering

Figure 2.26 shows the gain-corrected measurements for neutron scattering on ^{nat}V . The spectra are shown when the ^{nat}V is both included ($^{nat}\text{V}_{\text{in}}$) and removed ($^{nat}\text{V}_{\text{out}}$) from the experimental setup. The 0.764 MeV full-deposition peak is clearly evident. The wall effects are also visible. The **Geant4** simulation reproduces the measured curves well with the limitation of the shaping-time effects which result in the asymmetry of the peak, see Appendix A.1. The simulation of the $^{nat}\text{V}_{\text{in}}$ data was normalized to the height of the full-deposition peak. From the analytical calculations, the incident flux from the thermalizer is ~ 1800 n/s/cm², from which ~ 70 n/s/cm² are thermalized and scattered on ^{nat}V . When corrected by the solid angle of the detector from the ^{nat}V foil, fewer than 5 n/s will hit the detector due to the neutron scattering. Given that the measured “background” (the $^{nat}\text{V}_{\text{out}}$ setup) was ~ 70 n/s, the neutron scattering effect is expected to be less than 10% of all the events. In fact, from all the measurements with the same solid angle, 5% of the overall events originated from neutron scattering in ^{nat}V . This was also predicted by the simulations for this case. The measurements also show the potential of such a monitor for both low-rate applications and in the presence of a large background flux.

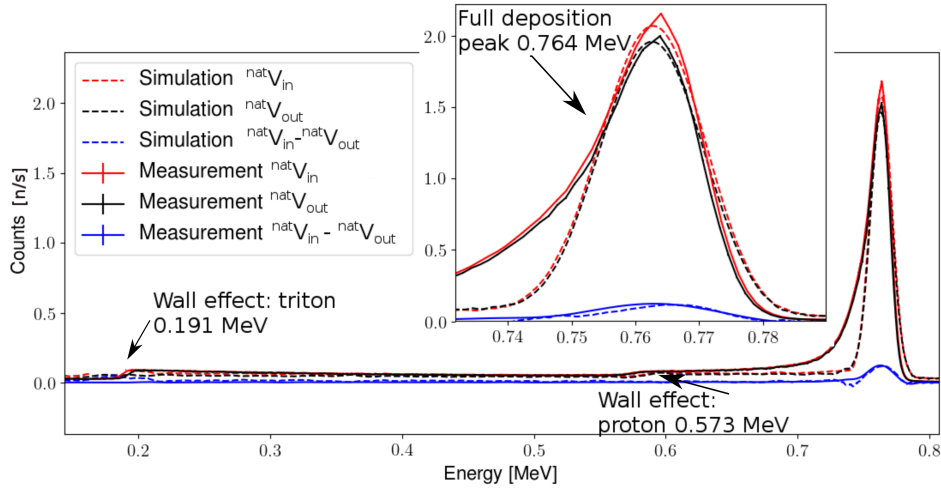


Figure 2.26. Neutron scattering on ^{nat}V . The blue curve represents the scattered neutrons. The inset shows the full-deposition peak. The simulated curves reproduce the data well.

The clear presence of the full-deposition peak over all measured spectra and the preservation of the $\frac{\text{natV}_{\text{in}}}{\text{natV}_{\text{out}}}$ ratio clearly demonstrated that the events were neutrons and that they originated from neutron scattering on the ^{nat}V foil.

2.5 Summary

At the conclusion of the calibration efforts, results from the absorption-based and scattering-based BM were carefully evaluated. It was concluded that an absorption-based BM at a neutron BL would be difficult to calibrate. Reasons for this difficulty include:

- The number of de-excitation events is not constant over time. In fact, it is only constant in the limit of constant neutron beam flux incident on the ^{nat}V foil.
- The number of activated atoms depends on the incident beam flux, which is in general not constant.
- The lead shielding required for the γ -ray detectors would be difficult to fit in the allocated volumes designated for BMs.
- There is no possibility for precise timing information as the decay constant is 221 s.

In contrast, the BM based upon scattering had the following positive attributes:

- In the limit of a constant beam, the number of scattered events is constant over time. Unlike the de-excitation events, when the beam is on or off, the response is immediate.
- Since γ -rays can be rejected by applying a suitable threshold, only boron shielding is needed, which allows more than one detector in an allocated volume. Symmetric responses of multiple detectors may be used to control the positioning of the beam.

Despite all the difficulties associated with having an isotropic source of neutrons, the proof of concept was verified.²⁷ It was thus decided that the absorption approach, while potentially useful for background characterization and dosimetry purposes, was not sufficiently of interest for continued investigation. The remainder of this thesis thus focuses on further investigation of the scattering approach.

²⁷In a more controlled environment where the neutron beam will be precisely defined (at the actual BL), the scattering-based BM results are anticipated to improve dramatically.

3 Commissioning at Helmholtz-Zentrum Berlin

3.1 Facility overview

Helmholtz-Zentrum Berlin consists of two large-scale facilities for scientific research: research reactor BER II for neutron experiments and synchrotron-radiation source BESSY II. BER II is located in Berlin Wannsee and has over 20 experiment stations, 10 of which are currently in use. All the measurements reported on here were performed at BER II. Figure 3.1 shows an overview of the BER II facility. Beamlines V17, a detector test station and V20, the ESS test beamline, were employed.

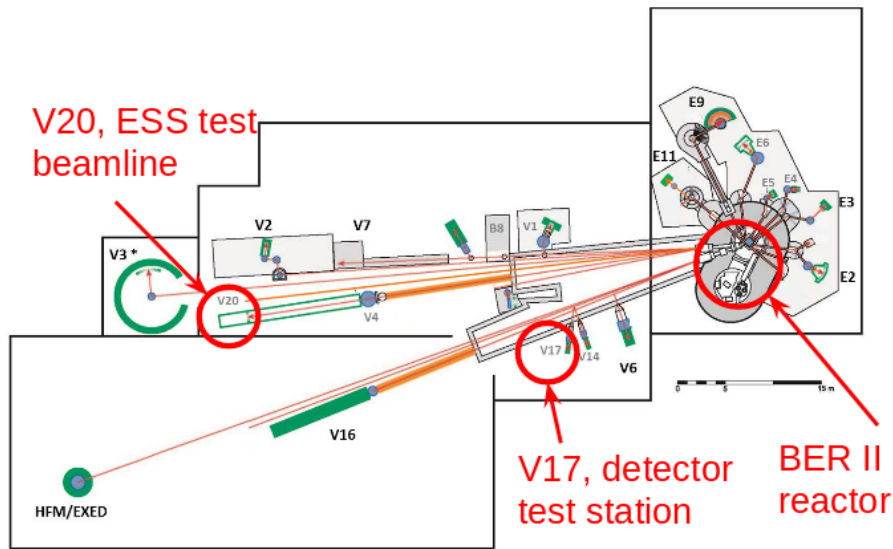


Figure 3.1. Overview of the BER II reactor at Helmholtz-Zentrum Berlin. The V17 and V20 beamlines used for the measurements reported on here are shown.

3.2 Apparatus

3.2.1 Beamlines

V17 [38] boasts a monochromatic neutron beam, created using a $8 \times 1 \text{ cm}^2$ pyrolythic graphite wafer slab that is 4 mm thick.²⁸ The approximate flux measured with a ^3He detector at the upstream end of the beamline is $2.3 \cdot 10^3 \text{ n/cm}^2/\text{s}$ [38]. The beam can be collimated by moving two sets of slits in the laboratory x- and y- directions in or out.

V20 [40] boasts variable settings for both the flux and wavelength of the neutron beam, see Fig. 3.2. V20 is designed to mimic the ESS pulse structure using several counter-rotating double-chopper systems. The ESS Source Chopper is calibrated to provide 2.86 ms pulse-length bunch with a repetition rate of 14 Hz. This emulates the ESS accelerated-proton beam which is directed onto the ESS tungsten target. After the source chopper, a system of Wavelength Frame Multiplication (WFM) choppers allow for the selection of a wavelength (energy) band. The

²⁸Pyrolythic graphite is a form of synthetic graphite used to monochromate the neutron beam according to Bragg's law [39].

wavelengths can vary between 1.8 Å and 10.2 Å. Neutron-wavelength resolution at this point is rather low (4.2%), so additional Wavelength-Band (WB) choppers are used. This set of choppers “slices” the beam pulse into six sub-pulses which enables tunable wavelength resolution. In this work, only the settings of the ESS Source Chopper (from now on referred to as choppers 1 and 2) and the WB Chopper (from now on referred as choppers 3 and 4) were varied.

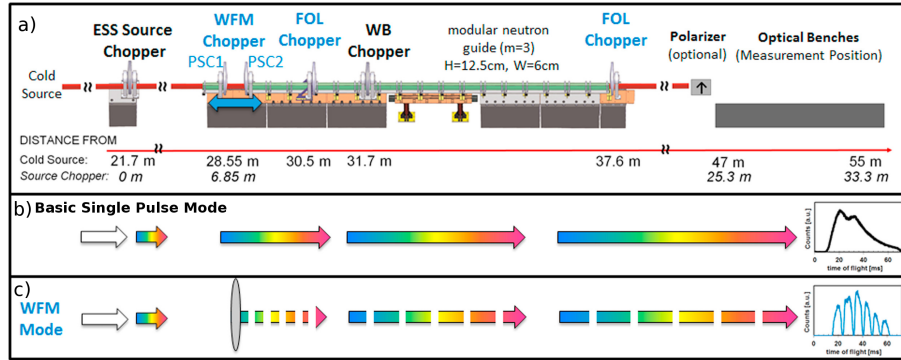


Figure 3.2. Layout of V20. (a) Choppers. The Source Chopper System consists of the ESS Source Chopper and a wavelength-band (WB) chopper. (b) Illustration of the basic single-pulse mode, where the measurement position defines the wavelength (energy) resolution and a continuous spectrum is recorded at the detector. (c) Illustration of the six-fold Wavelength Frame Multiplication (WFM) mode, where the spectrum is divided into sub-frames that are separated in TOF, but overlap in wavelength. Figure and description from Ref. [40].

3.2.2 Data-acquisition system

Figure 3.3 shows the DAQ system employed for the ^3He detectors. This setup was used at both the V17 and V20 beamlines. Operated at +1275 V, each detector produced a positive current pulse that was passed to a Cremat preamplifier [41]. From the preamplifier, two of the signals were passed to NIM ORTEC 673 amplifiers/shapers [42] while the other two were passed to Tennelec amplifiers/shapers [43]. A Rhode & Schwartz [34] oscilloscope was used to visually monitor the pulses periodically. The amplified and shaped pulses were passed to a FAST ComTec MCA4 [44]. The MCA integrated the current pulses to yield the charge corresponding to each event and binned these charges resulting in histograms that were stored for subsequent offline analysis.

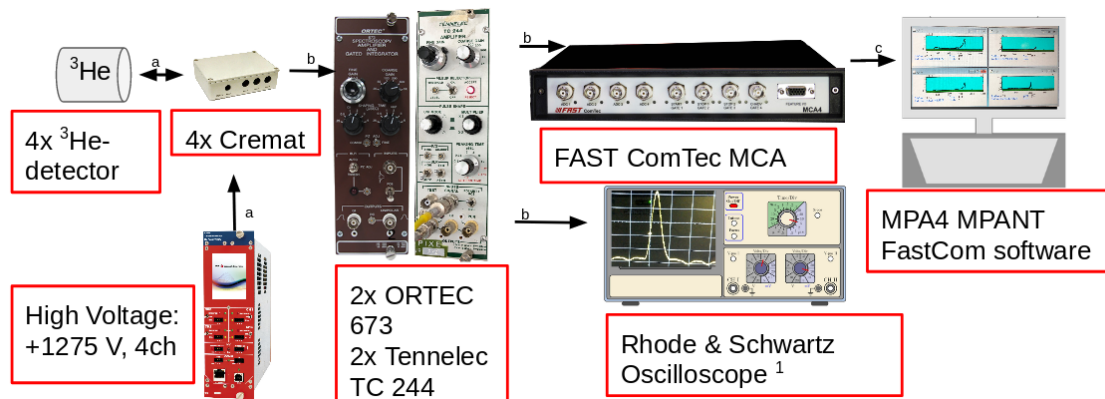


Figure 3.3. DAQ system for the ^3He detectors. a - HV cable, b - BNC cable, c - MCA-USB link. From left: four channels of HV power supply are connected to four preamplifiers which are connected to the base of each of the four detectors. The current pulse from the preamplifier is then amplified, shaped and passed to the MCA. The DAQ software histograms and displays the resulting spectra.

Furthermore, a fission chamber purchased from LND, Inc. [45] was used as a reference neutron-beam monitor for the V17 measurements.

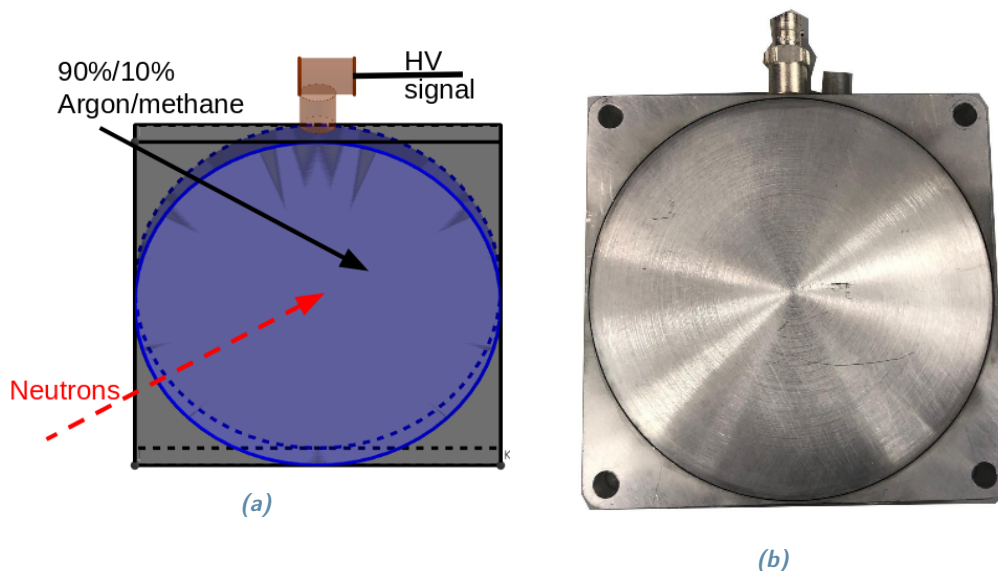


Figure 3.4. Fission chamber from LND. a) Overview: The incident neutrons (red) hit the active area (blue). The fission products are collected on the cathode/anode. b) Photograph.

The fission chamber relies upon induced fission in a neutron-rich material, see Eq. 3.2.1.



These detectors are essentially ionization chambers coated with fissionable material. This chamber contained 13 mg of ${}^{235}\text{U}$ and was filled with 90%/10% Argon/methane gas. The detection depth was 19.1 mm.

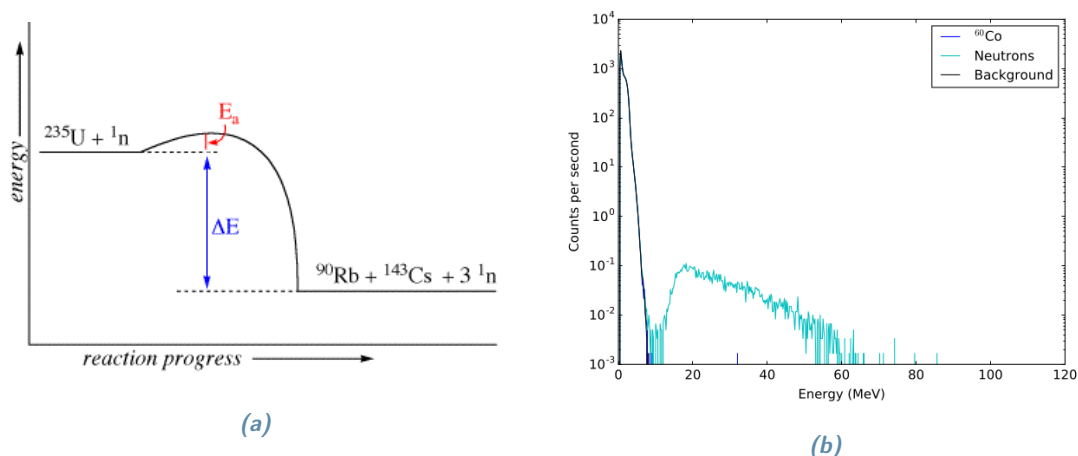


Figure 3.5. Fission-chamber response. (a) Principle of operation. (b) Typical response adapted from Ref. [46].

Figure 3.5 shows the typical response of a fission chamber. The fission products, as an example in this case ${}^{90}\text{Rb}$ and ${}^{143}\text{Cs}$, ionize the gas. The secondary ions are collected on the cathode and anode resulting in current pulses which may be analyzed.

3.3 Measurements and analysis

Figure 3.6 shows the experimental setup for neutron scattering on ^{nat}V . This setup was the same for both beamlines. ^{nat}V samples with several different dimensions (recall Table 2.4) were placed at the center of the setup and aligned with a laser. The ^3He detectors were placed around the ^{nat}V foil and connected to readout channels 1-4 as shown. Save for the entrance/exit windows corresponding to the ^{nat}V foils, the entire setup was shielded with a 3 mm thick Mirrobor [47] mask (B_4C) to reduce the background sensitivity of the device.

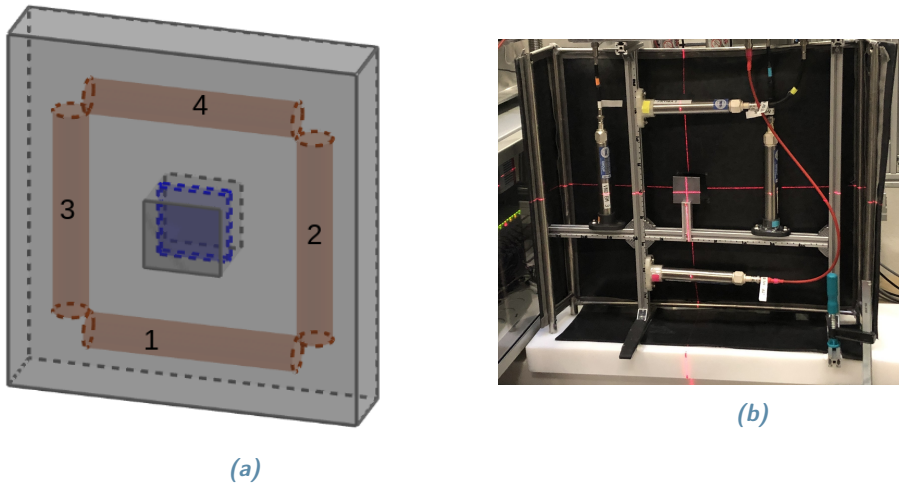


Figure 3.6. Setup for the ^{nat}V neutron-scattering measurements. (a) Sketch. ^{nat}V samples (blue) are surrounded by four ^3He detectors (brown). The entire setup was shielded by a B_4C mask (grey) with a window corresponding to the ^{nat}V samples in the center. (b) Photograph of the experimental setup with the front part of B_4C shielding (black) removed. The ^3He detectors (silver) surround the ^{nat}V sample. The laser alignment is shown in red.

V17

Figure 3.7 shows the experimental setup for neutron scattering on ^{nat}V at V17. The reference fission chamber was placed upstream of the ^{nat}V foil. The monochromatic neutron beam was collimated using two sets of slits. While the first set of slits was fixed at $3 \times 3 \text{ cm}^2$, the opening between the second set of slits was varied to study the response of the ^3He detectors which comprised the prototype BM as a function of neutron beam intensity on the ^{nat}V sample. Table 3.1 shows the complete set of neutron-scattering measurements. Table 3.2 shows the complete scan of the settings used for each of the measurements and the corresponding calculated neutron rate incident upon the ^{nat}V foil. For each measurement, many datafiles were obtained. The files were stored in increments of 90 s.

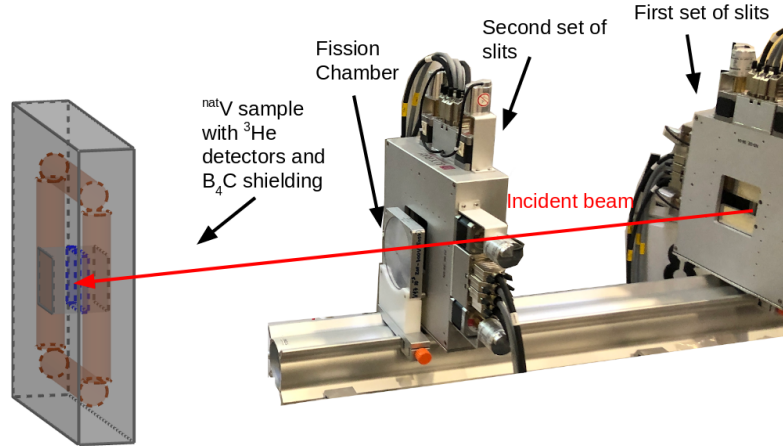


Figure 3.7. Beamline at V17. The incident beam (red) passes from the right to the left through two sets of (x,y) slits and a fission-chamber monitor before striking the ^{nat}V sample (blue).

Table 3.1. Neutron-scattering measurements at V17.

Run no.	Thickness [mm]	Fission Chamber	Duration [h]
1	3.15	Yes	4
2	3.15	No	26
3	1.00	No	5
4	0.20	No	10
5	0.20	No	15
6	0.125	No	10
7	0.125	No	15
8	0.040	No	14
9	No ^{nat}V	No	13

Table 3.2. Slit openings and the corresponding flux.

Slit X opening [mm]	Slit Y opening [mm]	Area A [mm ²]	I [10^3 n/s] = $2.3 \cdot 10^3 A$
0	0	0	0
2	2	4	0.1
4	4	16	0.4
6	6	36	0.8
8	8	64	1.5
10	10	100	2.3
12	12	144	3.3
14	14	196	4.5
16	16	256	5.9
18	18	324	7.5
20	20	400	9.2
22	22	484	11.1
24	24	576	13.2
26	26	676	15.5
28	28	784	18.0
30	30	900	20.7

Figure 3.8 shows the data-analysis sequence for the V17 measurements. Since the configuration of the slits was changed every 20 min but the measurements were stored every 90 s, a sorting algorithm was applied to distinguish between the slit settings. Once the datafiles were sorted, the runs were summed, energy calibrated and the resulting spectra were integrated. The rate in a ^3He detector of the prototype BM for each slit setting was plotted as a function of the neutron-beam intensity corresponding to the illumination area according to Table 3.2, see the thumbnail. The resulting spectrum is discussed in detail in Section 3.4.1.

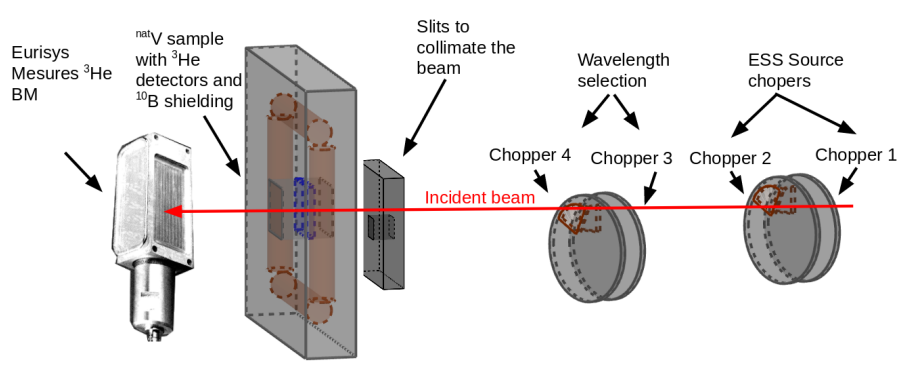


Figure 3.9. Beamline at V20. The incident beam (red) passes from right to the left through two sets of choppers and (x,y) slits before striking the ^{nat}V sample (blue). The residual beam is monitored with an invasive ^3He BM.

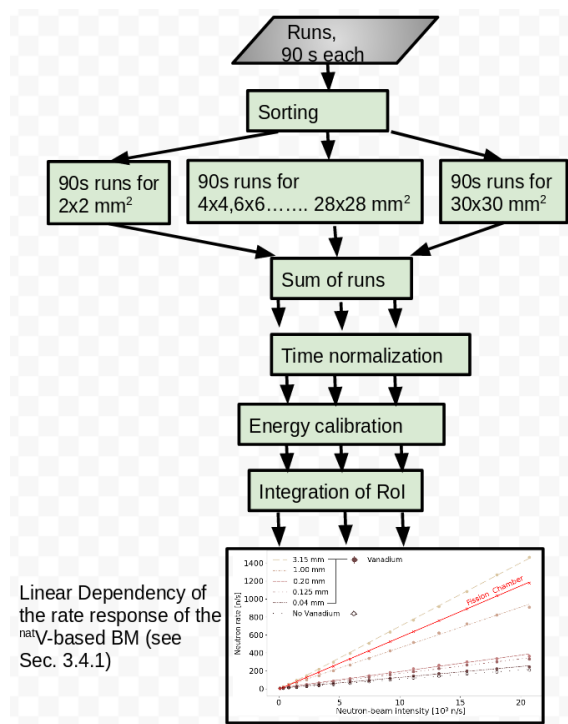


Figure 3.8. The analysis of the V17 data. The grey diamonds represent input and the green boxes represent processing. The resulting spectrum shown as a thumbnail is discussed in detail in Sec. 3.4.1.

V20

Figure 3.9 shows the experimental setup for neutron scattering on ^{nat}V at V20. The reference Eurisys Mesures ^3He BM was placed downstream of the ^{nat}V foil. The neutron beam was collimated using a set of slits with the opening fixed at $3 \times 3 \text{ cm}^2$. The phase opening of choppers 1, 3 and 4 were set at values of 0° , -42° and 157° respectively. This corresponded to a 3.0 \AA ($\sim 9 \text{ eV}$) wavelength setting. The phase of chopper 2 was varied to study the response of the ^3He detectors in the prototype BM as a function of neutron-beam intensity on the ^{nat}V sample maintaining the same illumination area. Table 3.3 presents an overview of the measurements performed at V20.

Table 3.3. Neutron-scattering measurements at V20. A portion of the measurements at V20 which were analyzed are shown. Ch2 stands for the Chopper 2 angle setting.

Run	Ch2 [°]	^{nat} V [mm]	Run	Ch2 [°]	^{nat} V [mm]	Run	Ch2[°]	^{nat} V [mm] ± 20 μm
1	40	3.15	22	30	No ^{nat} V	43	36	0.125
2	40	No ^{nat} V	23	29	3.15	44	35	0.125
3	39	3.15	24	29	No ^{nat} V	45	34	0.125
4	39	No ^{nat} V	25	28	3.15	46	33	0.125
5	38	3.15	26	28	No ^{nat} V	47	32	0.125
6	38	No ^{nat} V	27	27	3.15	48	31	0.125
7	37	3.15	28	27	No ^{nat} V	49	30	0.125
8	37	No ^{nat} V	29	26	3.15	50	29	0.125
9	36	3.15	30	26	No ^{nat} V	51	28	0.125
10	36	No ^{nat} V	31	25	3.15	52	27	0.125
11	35	3.15	32	25	No ^{nat} V	53	26	0.125
12	35	No ^{nat} V	33	24	3.15	54	25	0.125
13	34	3.15	34	24	No ^{nat} V	55	24	0.125
14	34	No ^{nat} V	35	23	3.15	56	23	0.125
15	33	3.15	36	23	No ^{nat} V	57	22	0.125
16	33	No ^{nat} V	37	22	3.15	58	31	0.02
17	32	3.15	38	22	No ^{nat} V	59	31	0.04
18	32	No ^{nat} V	39	40	0.125	60	31	0.20
19	31	3.15	40	39	0.125	61	31	1.00
20	31	No ^{nat} V	41	38	0.125	62	31	rod
21	30	3.15	42	37	0.125			

Figure 3.10 shows the data-analysis sequence for the V20 measurements. The spectra were energy calibrated and integrated. The neutron rate in a ³He detector of the prototype BM for each slit setting was plotted as a function of the flux corresponding to the absolutely calibrated ³He Eurisys Mesures BM. The resulting spectra are discussed in detail in Section 3.4.2.

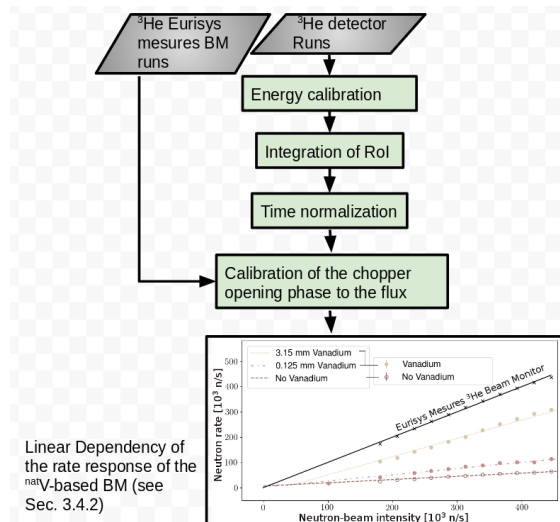


Figure 3.10. The analysis of the V20 data. The grey diamonds represent input and the green boxes represent processing. The resulting spectrum shown as a thumbnail is discussed in detail in Sec. 3.4.2.

3.4 Results

3.4.1 V17

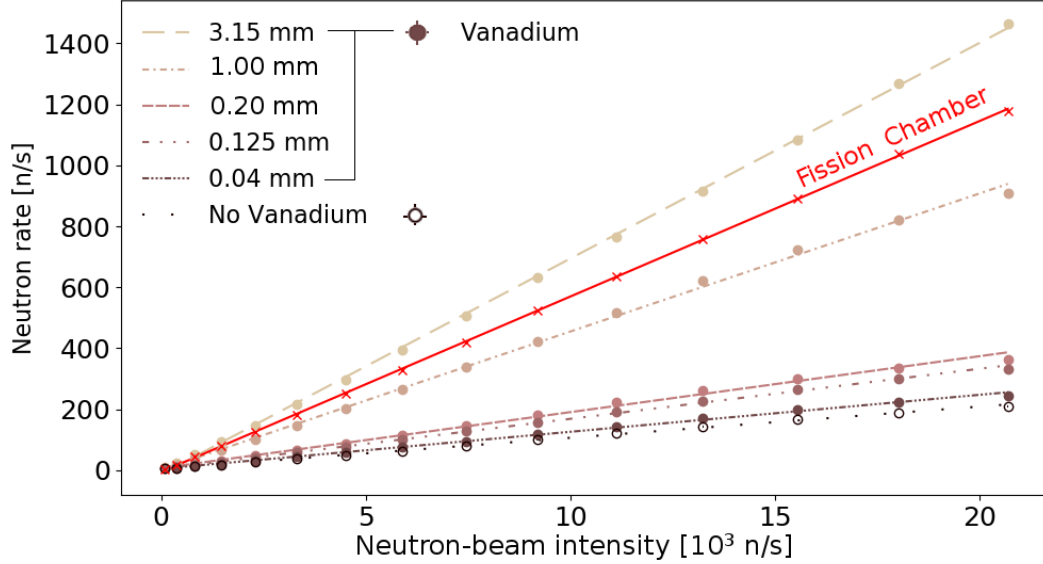


Figure 3.11. Prototype beam-monitor results for V17. Neutron rate in a ^3He detector as a function of neutron-beam intensity. The intensity was varied by changing the $^{\text{nat}}\text{V}$ foil illumination area. Filled points: rate in a ^3He detector with $^{\text{nat}}\text{V}$ present. Open points: rate in a ^3He detector with $^{\text{nat}}\text{V}$ not present. The red x's and fitted line correspond to the measurements with the reference fission chamber. The linear relationship between the measured rate in the detectors and the beam intensity is clear.

Figure 3.11 shows the measured neutron rate in a ^3He detector of the prototype BM as a function of thermal-neutron beam intensity at V17 with and without the $^{\text{nat}}\text{V}$ foil in the beamline. The results shown are for the ^3He detector of the prototype BM placed 5 cm beam left of the center of the $^{\text{nat}}\text{V}$ foil.²⁹ Plotted statistical uncertainties are not visible. The relationship between measured rate and beam intensity is clearly linear for all of the foils. In general, the slope of the fitted line increases as the thickness of the foil increases, which is expected from Fig. 1.4 in Sec. 1.2.2. The fission-chamber curve lies slightly below the results for the 3.15 mm $^{\text{nat}}\text{V}$ foil. The fission chamber is known to attenuate the neutron-beam intensity by 4% [46]. Table 3.4 shows the theoretically calculated attenuation for different thicknesses of $^{\text{nat}}\text{V}$ foil for the conditions of V17 (3.35 Å).

Table 3.4. Theoretical neutron attenuation in $^{\text{nat}}\text{V}$ at V17.

$^{\text{nat}}\text{V}$ foil thickness [mm] ($\pm 20 \mu\text{m}$)	Attenuation [%]
3.15	28.0
1.00	9.9
0.20	2.1
0.125	1.3
0.04	0.4

Recall that a desirable characteristic of an invasive BM is that it affects the smallest portion

²⁹This was the detector with the highest statistics. Several other distances between the ^3He detectors and the centers of the $^{\text{nat}}\text{V}$ foil were measured with similar results. The neutron rate observed in the ^3He detector decreased with the increasing distance from the $^{\text{nat}}\text{V}$ foil as expected.

of the beam possible while monitoring it with a response that scales linearly with intensity. The 0.125 mm ^{nat}V foil attenuates the beam by $\sim 1\%$. Clearly, the relationship for the 0.125 mm foil remains linear over a reasonable range of beam intensity while disturbing 75% fewer beam neutrons than the fission chamber which is typically used to monitor the beam. The 0.04 mm foil performs equally linearly and the attenuation is reduced even further.

When the ^{nat}V was removed from the setup, a linear increase of the rate observed in the ^3He detectors resulted from an increase in beam intensity. In an ideal environment, where the ^3He detectors would be perfectly shielded and there would be no other materials in close proximity to the beamline, the $^{nat}\text{V}_{out}$ response would be zero. Ideal environments rarely exist. Further, every environment in which this type of BM is employed is likely to be unique. Thus, *in situ* background runs without the ^{nat}V foil in the beam would need to be performed on a case-by-case basis to obtain the background-corrected rate in the ^3He detectors. This is a relatively simple task. Regardless, since both rates scale linearly, the non-corrected rate can in principle be used for the calibration of the ^{nat}V -based BM.

3.4.2 V20

V20 prototype results first required the determination of the neutron-beam intensity as a function of chopper phase-angle opening.

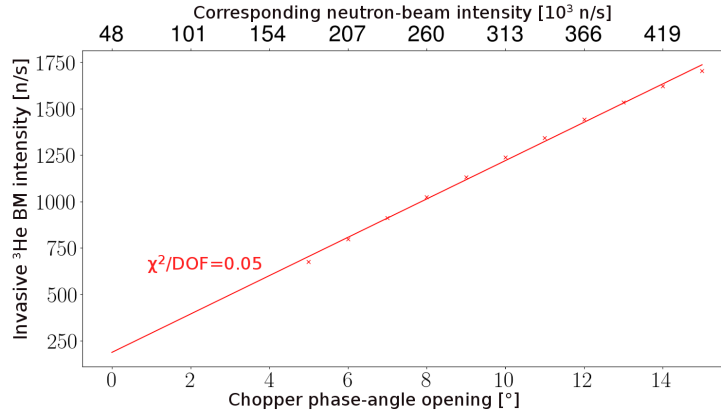


Figure 3.12. Chopper phase-angle opening and neutron-beam intensity.

The absolutely calibrated³⁰ reference ^3He BM from Eurisys Mesures was employed to relate the Chopper 2 phase-angle opening to the neutron-beam intensity. The measurements were performed when no ^{nat}V was present. Figure 3.12 shows the results of this calibration. The rate measured by the invasive ^3He BM was corrected for efficiency at each chopper phase-angle opening. The intensity-to-phase-angle relationship was determined using a linear fit to the data. The statistical uncertainties were lower than ± 2 n/s, which resulted in the statistical uncertainties in the corresponding intensities being smaller than ± 50 n/s. For example, a chopper phase-angle opening of 10° corresponded to a neutron-beam intensity of $(312\,860 \pm 50)$ n/s. The $\chi^2/dof=0.05$ of the fit over the chopper phase-angle opening range presented indicated that a linear functional relationship between the neutron-beam intensity and the ^3He BM count rate was appropriate.

³⁰The efficiency of this invasive BM was $3.9 \cdot 10^{-3}$.

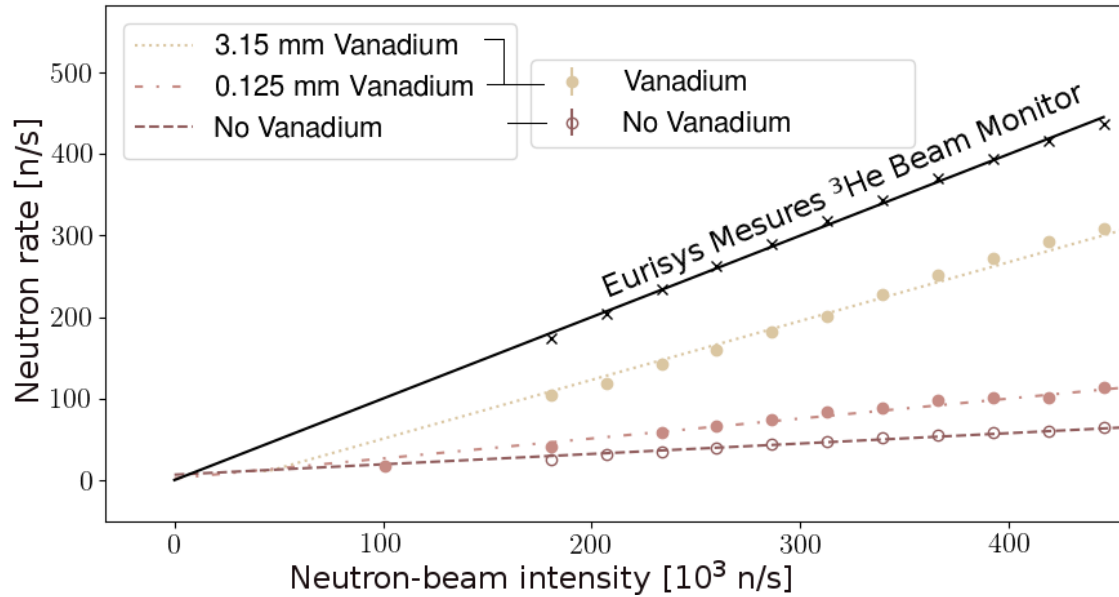


Figure 3.13. Prototype beam-monitor results for V20. Neutron rate in a ^3He detector of the prototype BM as a function of neutron-beam intensity. The intensity was varied by adjusting the chopper phase-angle opening. Filled points: rate in a ^3He detector with $^{\text{nat}}\text{V}$ present. Open points: rate in a ^3He detector with $^{\text{nat}}\text{V}$ not present. The black x's and fitted line correspond to the measurements with the Eurisys Mesures ^3He Beam Monitor. The linear relationship between the measured rate in the detectors and the beam intensity is clear.

Figure 3.13 shows neutron rate in a ^3He detector of the the measured prototype BM as a function of thermal-neutron beam intensity at V20 with 3.15 mm and 0.125 mm thick $^{\text{nat}}\text{V}$ foils and without $^{\text{nat}}\text{V}$ foil in the beamline. $3 \times 3 \text{ cm}^2$ of the foil were illuminated. The results shown are for the ^3He detector of the prototype BM placed 5 cm beam left of the center of the $^{\text{nat}}\text{V}$ foil.³¹ Statistical uncertainties are not visible in the plot. The relationship between measured rate and beam intensity is clearly linear for both of the foils. Again, the slope of the fitted line increases as the thickness of the foil increases, which is expected from Fig. 1.4 in Sec. 1.2.2. Just as in case of V17, when the $^{\text{nat}}\text{V}$ was removed from the setup, a linear increase of the rate observed in the ^3He detectors resulted from an increase in neutron-beam intensity. At V20, the highest measured intensity was $\sim 600 \cdot 10^3 \text{ n/s}$ for which the ^3He detectors did not show any sign of saturation.

³¹ Again, this was the detector with the highest statistics. Several other distances between the ^3He detectors and the centers of the $^{\text{nat}}\text{V}$ foil were measured with similar results. The neutron rate observed in the ^3He detector decreased with the increasing distance from the $^{\text{nat}}\text{V}$ foil as expected.

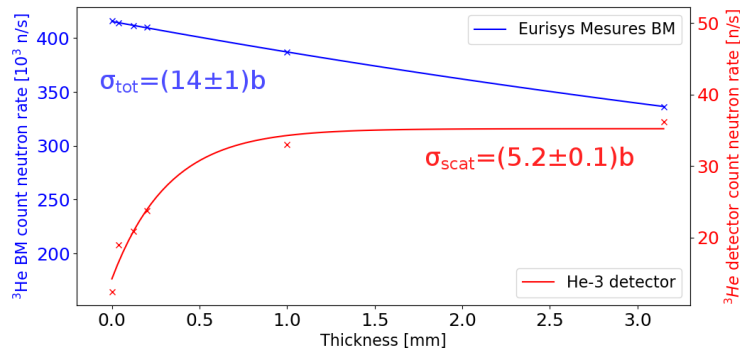


Figure 3.14. Absorption and scattering cross section extracted from the V20 data. Fit to the transmitted intensity recorded by the Eurisys Mesures invasive ^3He BM is shown in blue. Fit to the scattered events recorded by ^3He detector of the prototype BM is shown in red.

Figure 3.14 shows the dependence of the transmitted neutron-beam rate (blue) and scattered neutron-beam rate (red) as a function of the thickness of the $^{\text{nat}}\text{V}$ foil. The chopper opening for all these measurements was fixed at 14° , recall Fig. 3.12. Thus, the neutron-beam intensity was fixed at $I_0 = (418\,820 \pm 50)$ n/s and the thickness of the $^{\text{nat}}\text{V}$ foils was varied. The blue crosses show the neutron rate recorded by the ^3He Eurisys Mesures invasive ^3He BM for the six different thicknesses of $^{\text{nat}}\text{V}$ foils. The blue fitted function for the transmitted neutron rate has exponential dependency, recall Eq. 1.2.1. The total interaction cross section estimated from this fitted function was (14 ± 1) b. The red crosses show the rate of scattered neutrons recorded by a ^3He detector of the prototype BM placed 5 cm beam left of the center of the $^{\text{nat}}\text{V}$ foil. From the fitted function, the scattering cross section was determined to be (5.2 ± 0.1) b. This is in excellent agreement with the accepted value of 5.1 b [14]. Finally, by subtracting the scattering cross section from the total interaction cross section, an absorption cross section of $(\sim 9 \pm 1)$ b may be extracted, which is consistent with the expected value at a wavelength ~ 3 Å, see Fig. 1.5.

From the transmission measurements, the attenuation in each $^{\text{nat}}\text{V}$ foil was estimated. This was done by expressing ratio of I_{foil}/I_0 where I_{foil} is the intensity recorded by the Eurisys Mesures invasive ^3He BM for every thickness and I_0 is the intensity recorded by the Eurisys Mesures invasive ^3He BM when the $^{\text{nat}}\text{V}$ was removed from the setup. The results are summarized in Table 3.5.

Table 3.5. Measured neutron attenuation in $^{\text{nat}}\text{V}$ at V20.

$^{\text{nat}}\text{V}$ foil thickness [mm]	Measured attenuation [%]
3.15	19.0
1.00	7.0
0.20	1.4
0.125	1.1
0.04	0.5

3.5 Summary

At the conclusion of the commissioning efforts, the results from the measurements at beamlines V17 and V20 were carefully evaluated. It was concluded that the prototype $^{\text{nat}}\text{V}$ -based BM is already a fully functioning BM. In particular, the prototype has been successfully employed over a wide range of neutron-beam intensities. The measured responses were convincingly linear as a function of variations in neutron-beam intensity. These variations were achieved by changing both the beam-spot size and chopping. The thicknesses of the $^{\text{nat}}\text{V}$ foil which appear most promising

are 0.04 mm and 0.125 mm. For example, at a wavelength of 3 Å, the beam attenuation for the 0.125 mm foil is ~1% while for the 0.04 mm foil, it is ~0.5%. Attenuation decreases with decreasing wavelength, so for 25 meV thermal neutrons with wavelength 1.8 Å at ESS, the attenuation is guaranteed to be even lower. Further, this attenuation is already even lower than the vast majority of the commonly used BMs. It appears that the concept is sound and worth further detailed development for the purpose of deployment at ESS.

4 Closing Remarks

4.1 Summary

The goal of this thesis was to investigate the feasibility of an invasive quasi-parasitic thermal-neutron BM for beam diagnostics at high flux BLs at spallation sources in close proximity to choppers. The BM was to be based upon a thin ^{nat}V foil and standard ^3He proportional counters. Both absorption-based and scattering-based BMs were conceived. The project was divided into a calibration phase performed at the STF and a commissioning phase performed at HZB. The goal of the calibration phase was to determine which of the two methods was the most promising. At the conclusion of the calibration phase, results from the absorption-based and scattering-based BMs were critically evaluated.

The BM based upon absorption had the following attributes which raised concerns:

- The number of activated atoms and thus de-excitation γ -ray events is only constant in the limit of constant neutron beam flux incident on the ^{nat}V foil. This makes monitoring the beam much more difficult as the properties of the monitor are continuously changing.
- The rather substantial amount of lead shielding needed to protect the γ -ray detectors from the intense γ -ray backgrounds associated with spallation would be difficult to fit in the allocated volumes designated for BMs at the BLs in question.
- There is no possibility for beam pulse timing information as the decay constant on the per-pulse scale for $^{52}\text{Cr}^*$ is 221 s, far too long for any fast feedback applications.

The BM based upon scattering had the following attributes which were considered advantageous:

- In the limit of a steady neutron beam, the number of scattered events is also steady. Response in hardware to the changes in the beam is immediate as there is no decay constant to consider.
- Since γ -rays can be rejected easily by applying a suitable threshold to the detectors, only boron shielding is needed to shield them from unwanted thermal-neutron background. This potentially allows for more than one BM in an allocated volume at a BL in question.
- Uniform responses of multiple symmetrically aligned detectors may be used to monitor and even control the positioning of the beam if a suitable fast-feedback systems are developed.

It was determined that an absorption-based BM at a neutron BL would be difficult both to calibrate and employ while a scattering-based BM at a neutron BL would be far easier both to calibrate and to employ. It was thus decided that the absorption approach, while potentially useful for background characterization and dosimetry purposes, was not of sufficient interest for continued investigation in the subsequent commissioning phase.

At the conclusion of the commissioning phase, results from the measurements at HZB BLs V17 and V20 for the scattering-based approach were critically evaluated. The BM was successfully employed with a linear response over a wide range of neutron-beam intensities. These variations in intensity were achieved by changing both the beam-spot size and the time structure of the beam using choppers. The thicknesses of the ^{nat}V foil which appear most promising are 0.04 mm and 0.125 mm, with attenuations at 3 Å of $\sim 0.5\%$ and $\sim 1.0\%$ respectively. While the attenuation of 1.8 Å neutrons (25 meV) at ESS will be even lower, this attenuation is already much lower than the vast majority of commonly used BMs. It was thus determined that the prototype ^{nat}V -based BM is already a fully functioning BM.

4.2 Conclusions

The scattering-based prototype employing a ^{nat}V foil and standard ^3He detectors in a configuration symmetric around the foil functions excellently as an invasive quasi-parasitic BM. This conclusion is based upon the minimal measured beam attenuation with demonstrated linearity over a neutron-beam intensities ranging from 100–500K n/s. As variations in the neutron-beam intensity were obtained by both varying the beam-spot size with slits as well as altering the time structure of the beam with choppers, confidence in the response performance of the BM to widely varying beam conditions is high. The definition of quasi-parasitic employed in this work was that the BM should attenuate no more than $\sim 1\%$ of the neutron beam. Based upon this definition, the maximum ^{nat}V foil thickness cannot exceed 0.125 mm, where the attenuation is 1.3% at 3 Å. As the prototype demonstrated both low neutron-beam attenuation and response linearity over a reasonable dynamic range, it appears that the concept is sound and worth further detailed development for the ultimate purpose of deployment at ESS.

4.3 Outlook

Further detailed development of the prototype is suggested for the ultimate purpose of deployment at ESS. These investigations should include:

- Simulating the HZB results.
- Determining the high-flux limitations of the device at facilities such as J-Parc or Dubna.
- Incorporating both time stamping and neutron-energy monitoring. This should be done at HZB, since the chopper settings there may be used to produce a neutron beam that closely resembles the ESS pulse.
- Performing long-term exposure measurements in intense fields of neutrons and γ -rays to benchmark the lifetime of the prototype. This benchmarking should result in an estimated performance stability over the lifetime of the device.
- Optimizing the thickness and mounting of the prototype-related shielding.
- Developing non-modular electronics fully dedicated to the prototype.

A ^3He Detector Studies

A.1 Shaping Time and resolution

To understand the shapes of the spectra from the ^3He detector, data were taken with 12 different settings for the amplifier/shaper shaping constant to study its effect on the energy resolution. These were recorded both when it was placed next to the bare neutron source and next to the thermalizer with the source inside. Figure A.1 shows the data-analysis sequence for dependence of the energy resolution on the shaping time of the amplifier. For each run, the shaping time

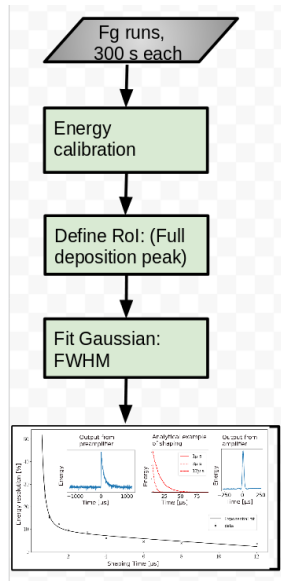


Figure A.1. Shaping-time analysis. Grey diamonds represent input and green boxes represent processing. The resulting spectrum shown as a thumbnail is discussed in detail in Fig. A.3.

was set and the collected data were energy calibrated. A Gaussian function was fitted to the full-deposition peak allowing the FWHM of the peak ΔE_{FWHM} for each of the shaping times to be approximated. The energy resolution R was determined according to:

$$R = \frac{\Delta E_{\text{FWHM}}}{E} \cdot 100\%, \quad (\text{A.1.1})$$

where E was the mean of the fitted Gaussian distribution.

Figure A.2 shows the thermal-neutron responses of the ^3He detector obtained using different amplifier shaping times. In general, as the shaping time increased, the full-deposition peak became narrower and the energy resolution increased. For the shortest shaping times ($0.75 \mu\text{s}$ and $1 \mu\text{s}$), the full-deposition peak was barely visible. In fact, the $0.75 \mu\text{s}$ spectrum does not even demonstrate wall effects (see the inset). In order to determine the shaping time for the best possible energy resolution, Gaussian functions were fitted to the spectra shown in Fig. A.2. From each FWHM, the energy resolution at 764 keV was calculated and plotted as a function of the shaping time.

Figure A.3 presents a discussion of the concept of amplifier shaping. The left inset shows a typical pulse leaving the preamplifier. This inset was generated by using the preamplifier signal obtained using a digital oscilloscope and applying Eq. A.1.2. The shaping amplifier shaped the signal from the preamplifier. According to the ORTEC 673 manual [33] (see also Ref. [48]), the

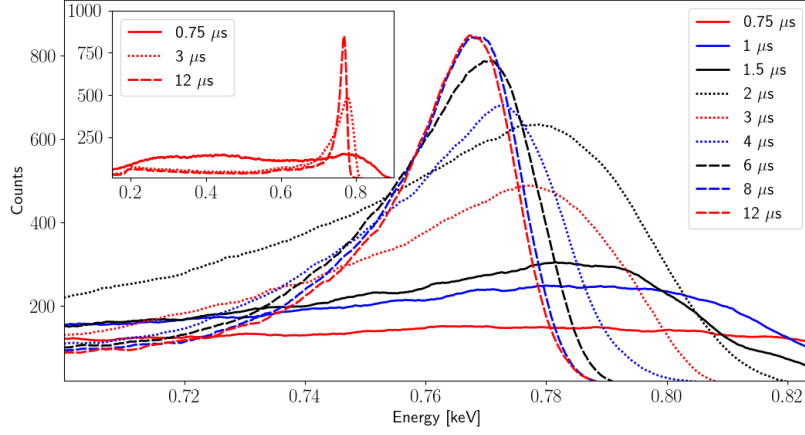


Figure A.2. Full-deposition peak as a function of shaping time.

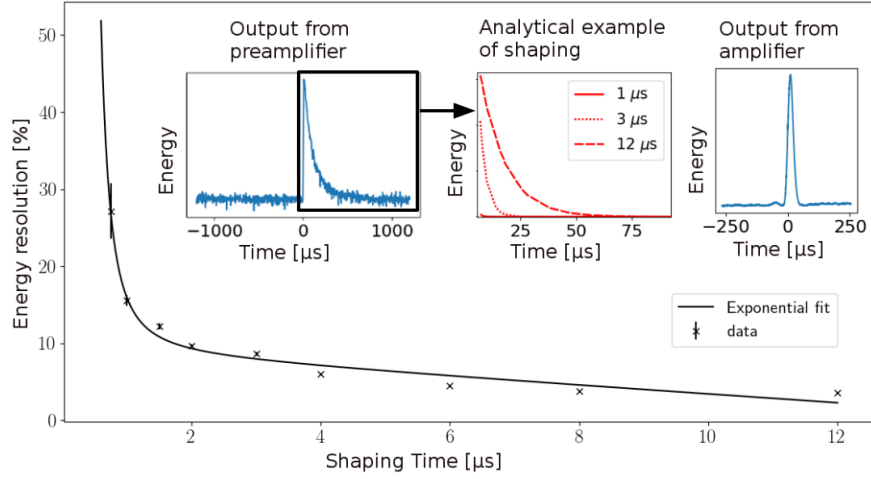


Figure A.3. Resolution of the full-deposition peak as a function of shaping time.

preamplifier signal V_0 was transformed according to:

$$V_{\text{out}}(t) = V_0 \cdot e^{-t/\tau}, \quad (\text{A.1.2})$$

where $V_{\text{out}}(t)$ was the output voltage at time t and τ was the amplifier-shaping time. The middle inset shows an analytical example of such a transformation on the data from the left inset for different shaping times. Finally, the right inset shows the post shaping-amplifier pulse. Since a change in V_0 will result in a change in V_{out} given by Eq. A.1.2, the resolution of the detector will have the same exponential dependency. The main panel of Fig. A.3 shows an exponential fit that was performed to the measured resolution data to illustrate the shaping-time dependence. The fit qualitatively describes the data well. Note that the provider of the ^3He detector states the resolution of the full-deposition peak to be 5%. It can be clearly seen that this level of energy resolution is reached at shaping times higher than 8 μs .

A.2 Simulated response

Figure A.4 shows the output of the Geant4 simulation when the $^{241}\text{Am}/^9\text{Be}$ source was placed within the thermalizer and the ^3He detector was placed in front of the large thermalizer opening. The red curve is the reference spectrum provided by Reuter Stokes. The Geant4 simulation is

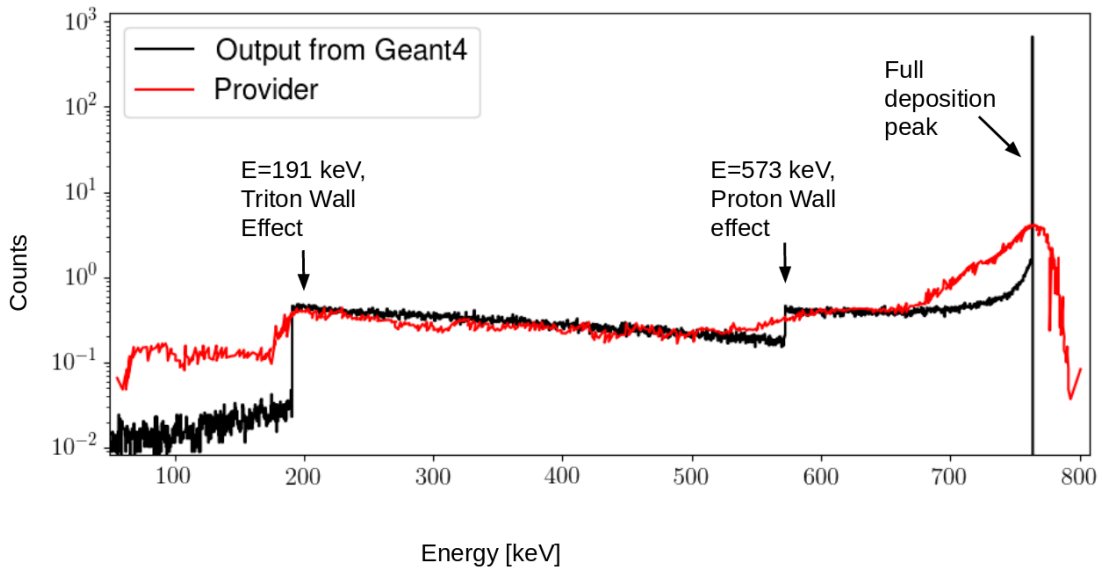


Figure A.4. Response of the ^3He detector. Simulated using Geant4 (black) and measured by the provider (red). Agreement is poor.

clearly "sharper" compared to the reference spectrum. This is due to the lack of "smearing" based upon detector energy resolution in the simulated spectrum.

The most common approach to smearing is to apply an energy-dependent energy resolution function to the simulation distribution. Each simulated event is smeared by the FWHM of a Gaussian distribution representing the energy-resolution function. The result of applying such a smearing algorithm to the simulated response is shown in Fig. A.5. The simulated spectrum provides an improved match in the lower-energy region, but the agreement with the full-deposition peak is still poor.

To better understand the difference between the resolution-smearred simulated response of the ^3He detector and the response measured by the provider, a new simulation algorithm was developed. While the majority of the stopping power of the ^3He gas is due to ionization, some of the stopping power is due to nuclear scattering. The algorithm was based upon the assumption that some of the stopping power of the ^3He gas was due to this nuclear component. The nuclear component of the stopping power is not deposited in the detector at these energies as the intact ^3He atom simply recoils. Figure A.6 presents a visualization of the regions of the particle track for which the probability of losing energy via nuclear scattering instead of ionization increases to a non-negligible level.

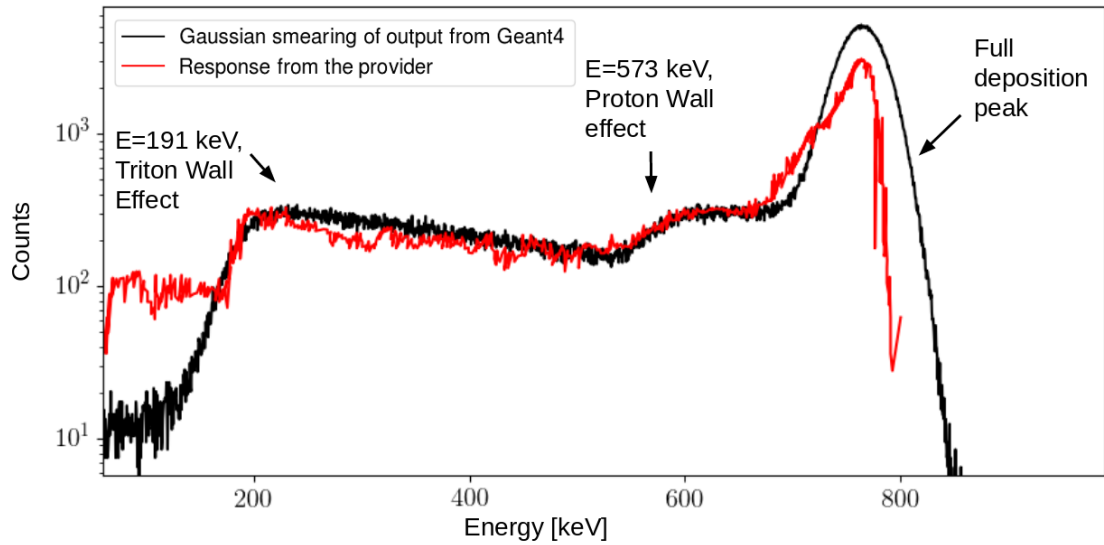


Figure A.5. Energy-resolution smeared response of the ^3He detector. Simulated using Geant4 (black) and measured by the provider (red). Agreement has improved in the wall regions.

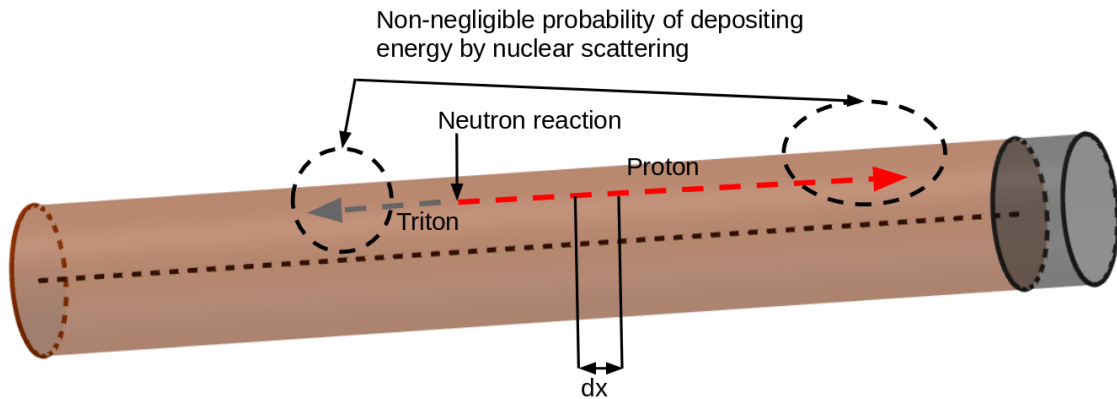


Figure A.6. Visualization of the ^3H and ^1H trajectories inside the ^3He detector. The tracks of the ^1H (red dashed line) and the ^3H (grey dashed line) are shown. The dashed circles highlight the end of the charged-particle paths where $\beta \rightarrow 0$ and nuclear scattering energy loss takes over from ionization energy loss.

Tanabashi [49] explains that for $0.01 < \beta < 0.05$ (where $\beta = \frac{v}{c}$), the Beta-Bloch equation [27] fails and semi-empirical methods [50] are necessary to explain the energy loss of the ^1H and the ^3H . Figure A.7 illustrates this semi-empirical evaluation. For the ^3H , the effect of the nuclear-scattering component of the energy loss is as large as that of the ionization component at 20 keV. For the ^1H , the effect of the nuclear-scattering component of the energy loss is as large as that of the ionization component at 10 keV.

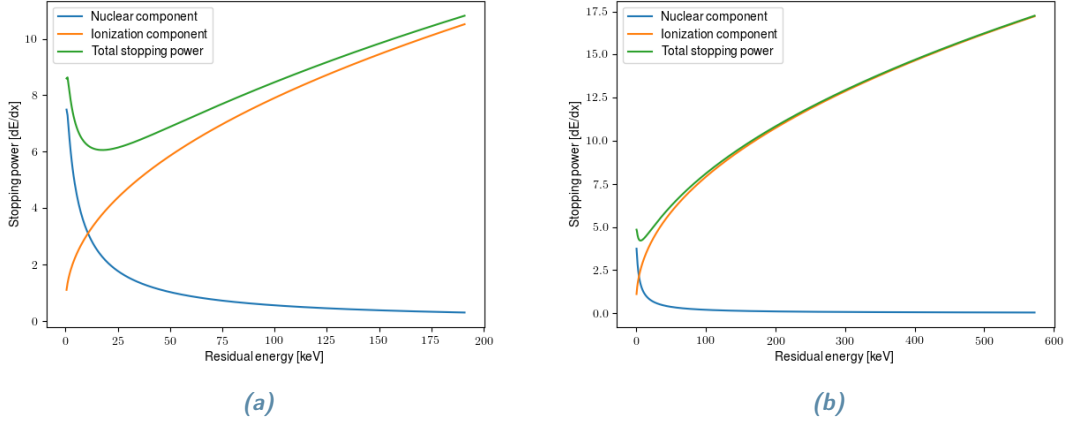


Figure A.7. Stopping powers of ${}^3\text{H}$ s and ${}^1\text{H}$ s in the ${}^3\text{He}$. The ionization component of the energy loss is shown in orange and the nuclear component is shown in blue. The green curve represents the total stopping power.

A new smearing algorithm was developed to include the nuclear-scattering energy loss effects, see Fig. A.8. The implementation was performed as follows.

- The Geant4 spectrum (black distribution in Fig. A.4) was divided into three sub-spectra: a ${}^1\text{H}$ sub-spectrum in the energy interval $[0.573, 0.764)$ MeV, a ${}^3\text{H}$ sub-spectrum in the energy interval $[0.191, 0.765)$ MeV and full-energy deposition sub-spectrum with energy 0.764 MeV.
- Consider the ${}^3\text{H}$ sub-spectrum³² and refer to Fig. A.8. Each of the ${}^3\text{H}$ events generated using Geant4 can have energies from 0 to 191 keV, depending on kinematics of the reaction. Consider a ${}^3\text{H}$ event that has 60 keV. A stopping power curve is generated in the range $(0, 60)$ keV and this energy range is divided into small steps. When the ${}^3\text{H}$ loses enough energy to cross the boundary between two steps, the normalized probability p_i of the energy being deposited due to ionization and the normalized probability p_n of the energy being deposited due to nuclear scattering were determined. The computer then generated a random number between 0 and 1. This output was used to determine if the differential energy loss was due to ionization or nuclear scattering. The process was then repeated for the next energy-loss step and the process continued until the particle stopped. In the end, the differential energies that were deposited due to ionization were summed and the original 60 keV event was placed in the corresponding energy bin.
- The process was then repeated for all the events in all the bins in the entire spectrum.

The results of the newly created algorithm compared to the response measured by the provider are shown in Fig. A.9. The area under the full-deposition peak is well approximated with the new algorithm. However, the simulation does not agree as well in the region below the full-deposition peak. Here, the standard approach of Gaussian smearing worked much better.

³²The ${}^3\text{H}$ spectrum is representative.

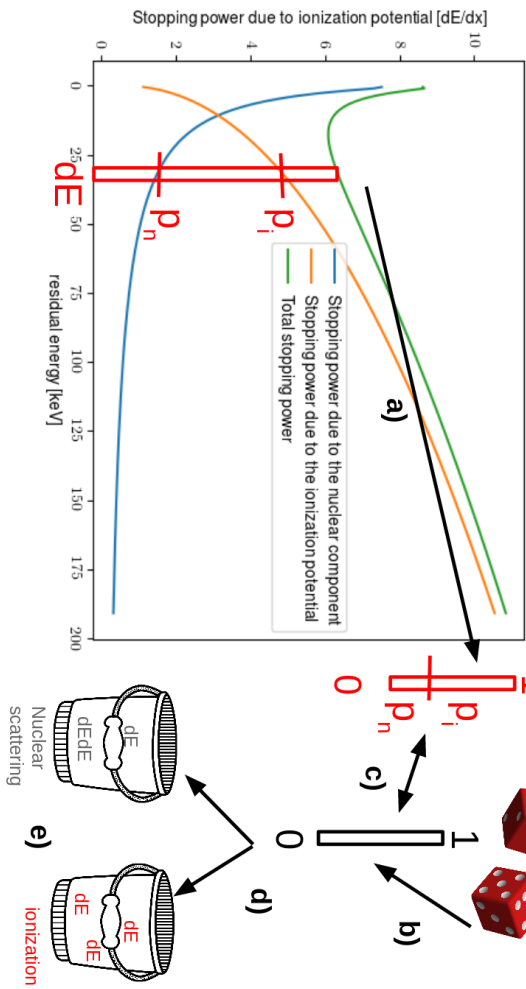
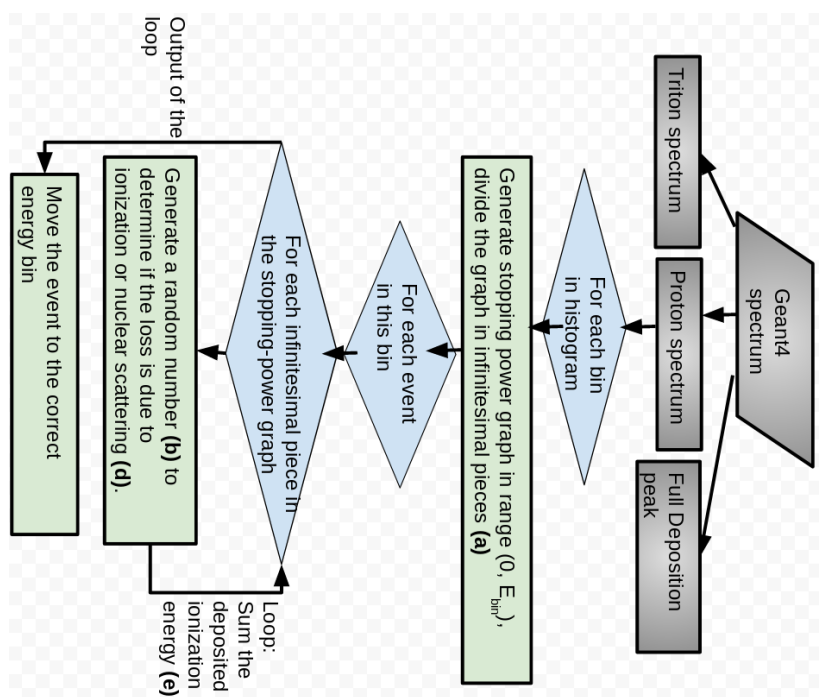


Figure A.8. Illustration of the custom-response algorithm. Left: Algorithm used to calculate the energy deposition of a ^3H in the detector. a) probabilities of nuclear scattering and ionization. b) computer-generated random number between 0 and 1 c) comparison to ionization probability. d) Differential energy loss due to nuclear scattering or ionization. e) Summation and incrementation of the histogram. Right: Algorithm flow chart. The simulated response generated using Geant4 is divided into a ^3H spectrum, ^1H spectrum and full-deposition peak (grey diamonds). Energy deposition via ionization and nuclear scattering is considered to be differential. Loops are represented in blue and the green boxes represent the commands inside the loops.



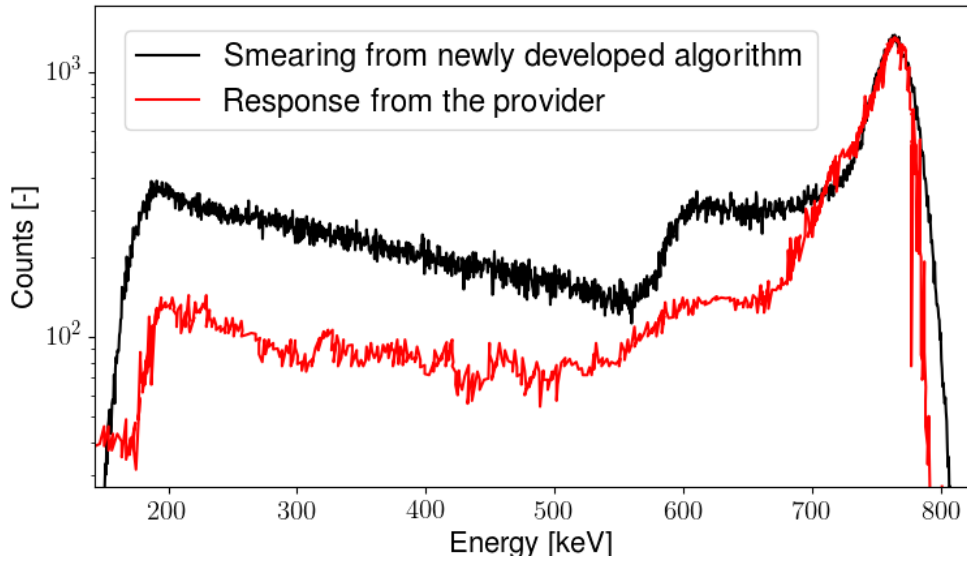


Figure A.9. Simulation-smeared response of the ^3He detector. Simulated using custom algorithm (black) and measured by the provider (red). Agreement has improved in the full-deposition region.

In a conclusion, the new algorithm redistributes the energies in the full-deposition peak to the lower-energy region. Compared to the crude approach of addressing resolution effects using Gaussian smearing, this approach matches the measured response better in the full-deposition region around 764 keV. It does not replicate the balance between the counts in the wall regions as well. More work beyond the scope of this thesis is necessary.

Bibliography

- [1] Steve Peggs. Technical Design of the ESS Facility. In *Proceedings, 4th International Particle Accelerator Conference (IPAC 2013): Shanghai, China, May 12-17, 2013*, page THPWO074, 2013.
- [2] Steve Peggs et al. *European Spallation Source Technical Design Report ESS-2013-001*. 04 2013.
- [3] J. R. Dunning, G. B. Pegram, G. A. Fink, D. P. Mitchell, and E. Segrè. Velocity of slow neutrons by mechanical velocity selector. *Phys. Rev.*, 48:704–704, Oct 1935.
- [4] European Spallation Source. The ess instrument suite – a capability gap analysis. <https://europeanspallationsource.se/instruments/capability-gap-analysis>, 2019. Accessed: 2019-04-03.
- [5] Kalliopi Kanaki. The beam monitors common project at ess. https://indico.esss.lu.se/event/1163/contributions/8878/attachments/8682/13152/ikon16_kanaki_bmcp.pdf, 2019. Accessed: 2019-04-03.
- [6] ISIS. Isis neutron and muon source. <https://www.isis.stfc.ac.uk>, 2019. Accessed: 2019-04-03.
- [7] Dr. Robert Bewley. Private commentation, 2018. ISIS Neutron and Muon Source, LET instrument scientist.
- [8] J. Mayers. The use of vanadium as a scattering standard for pulsed source neutron spectrometers. *Nuclear Instruments and Methods in Physics Research*, 221(3):609 – 618, 1984.
- [9] D.H. Day, D.A.G. Johnson, and R.N. Sinclair. The use of vanadium scattering to intercalibrate an array of thermal neutron detectors. *Nuclear Instruments and Methods*, 70(2):164 – 168, 1969.
- [10] D.I. Page. The phonon frequency distribution of vanadium. *Proceedings of the Physical Society*, 91(1):76–85, 1967.
- [11] A. T. STEWART and B. N. BROCKHOUSE. Vibration spectra of vanadium and a mn-co alloy by neutron spectrometry. *Rev. Mod. Phys.*, 30:250–255, Jan 1958.
- [12] C. M. Eisenhauer, I. Pelah, D. J. Hughes, and H. Palevsky. Measurement of lattice vibrations in vanadium by neutron scattering. *Phys. Rev.*, 109:1046–1051, Feb 1958.
- [13] Asha Goel, Sneha Mohan, and B. Dayal. Lattice dynamics of vanadium and niobium by a modified sharma-joshi model. *Physica B+C*, 96(2):229 – 236, 1979.
- [14] J.R. Granada, F. Kropff, and R.E. Mayer. On the thermal neutron scattering from polycrystalline vanadium. *Nuclear Instruments and Methods in Physics Research*, 189(2):555 – 559, 1981.
- [15] W. Dilg. Redetermination of the slow neutron scattering cross section for vanadium. *Nuclear Instruments and Methods*, 122:343 – 346, 1974.
- [16] Varley F. Sears. Neutron scattering lengths and cross sections. *Neutron News*, 3(3):26–37, 1992.
- [17] Goodfellow. Goodfellow supplier for materials. <http://www.goodfellow.com/>, 2010. Accessed: 2018-09-06.

- [18] T Kittelmann, I Stefanescu, K Kanaki, M Boin, R Hall-Wilton, and K Zeitelhack. Geant4 based simulations for novel neutron detector development. *Journal of Physics: Conference Series*, 513(2):022017, 2014.
- [19] Xiao-Xiao Cai and Thomas Kittelmann. Ncrystal : a library for thermal neutron transport. arXiv:1901.08890, 2019.
- [20] R. Hall-Wilton, K. Kanaki, V. Maulerova, I. Apostolidis, and S. Alcock. Common beam monitor project, 2018. doc. no: ESS-0502620.
- [21] J.W. Marsh, D.J. Thomas, and M. Burke. High resolution measurements of neutron energy spectra from ambe and amb neutron sources. *Nuclear Instruments and Methods in Physics Research Section A: Accelerators, Spectrometers, Detectors and Associated Equipment*, 366(2):340 – 348, 1995.
- [22] Julius Scherzinger, Ramsey Al Jebali, John Annand, Kevin Fissum, Richard Hall-Wilton, Sharareh Koufigar, Nicholai Mauritzson, Francesco Messi, Hanno Perrey, and Emil Rofors. A comparison of untagged gamma-ray and tagged-neutron yields from 241ambe and 238pube sources. 2016.
- [23] National Nuclear Data Center and Brookhaven National Laboratory. Nudat2.7. <https://www.nndc.bnl.gov/nudat2/chartNuc.jsp>, 2019. Accessed: 2019-04-03.
- [24] S. Agostinelli, J. Allison, K. Amako, J. Apostolakis, H. Araujo, P. Arce, M. Asai, D. Axen, S. Banerjee, G. Barrand, et al. Geant4—a simulation toolkit. *Nuclear Instruments and Methods in Physics Research Section A: Accelerators, Spectrometers, Detectors and Associated Equipment*, 506(3):250 – 303, 2003.
- [25] J. Allison, K. Amako, J. Apostolakis, P. Arce, M. Asai, T. Aso, E. Bagli, A. Bagulya, S. Banerjee, G. Barrand, et al. Recent developments in geant4. *Nuclear Instruments and Methods in Physics Research Section A: Accelerators, Spectrometers, Detectors and Associated Equipment*, 835:186 – 225, 2016.
- [26] M. Iji. Recycling of ic molding resin wastes from ic package production processes. In *Proceedings of International Symposium on Semiconductor Manufacturing*, pages 197–200, Sept 1995.
- [27] Glenn F. Knoll. *Radiation detection and measurement*. Wiley New York, 2nd ed. edition, 1989.
- [28] SCIONIX. Dedicated scintillation detectors. <https://scionix.nl/scintillation-crystals/#tab-id-4>, 2018. Accessed: 2018-09-24.
- [29] Kenneth S Krane, 1916 Halliday, David, and 1916-. Introductory nuclear physics Halliday, David. *Introductory nuclear physics*. New York : Wiley, rev. ed. [i.e. 3rd ed.] edition, 1987. Rev. ed. of: Introductory nuclear physics / David Halliday. 2nd ed. 1955.
- [30] Said Mughabghab. *Atlas of neutron resonances; 6th ed.* Elsevier, Amsterdam, 2018.
- [31] D. Mazed, S. Mameri, and R. Ciolini. Design parameters and technology optimization of 3he-filled proportional counters for thermal neutron detection and spectrometry applications. *Radiation Measurements*, 47(8):577 – 587, 2012.
- [32] Reuter Stokes. Reuter stokes. <https://www.industrial.ai/measurement-sensing/radiation-measurement/homeland-security-detectors/helium-3-gas-filled-proportional-detectors>, 2019. Accessed: 2019-04-03.
- [33] Ortec. *Model 673 Spectroscopy Amplifier and Gated Integrator Operating and Service Manual*. Ortec. Accessed: 2019-04-13.

- [34] Rohde & Schwartz. Rohde & schwartz. https://www.rohde-schwarz.com/se/home_48230.html, 2019. Accessed: 2019-03-21.
- [35] Materials Analysis Division AMETEK. Mca-8000d digital multichannel analyzer. <http://amptek.com/products/mca-8000d-digital-multichannel-analyzer/>, 2019. Accessed: 2019-04-03.
- [36] Ortec. *Model 142PC Preamplifier Operating and Service Manual*. Ortec. Accessed: 2019-04-13.
- [37] Ortec. *Model 276 Preamplifier Operating and Service Manual*. Ortec. Accessed: 2019-04-13.
- [38] Helmholtz-Zentrum Berlin. Detector test station, v17. <https://www.helmholtz-berlin.de>, 2019. Accessed: 2019-09-05.
- [39] M Adib, Neelofer Habib, M S. El-Mesiry, and M Fathallah. Characteristics of pyrolytic graphite as a neutron monochromator. *Energy and Environment Research*, 2, 04 2012.
- [40] R. Woracek, T. Hofmann, M. Bulat, M. Sales, K. Habicht, K. Andersen, and M. Strobl. The test beamline of the european spallation source – instrumentation development and wavelength frame multiplication. *Nuclear Instruments and Methods in Physics Research Section A: Accelerators, Spectrometers, Detectors and Associated Equipment*, 839:102 – 116, 2016.
- [41] Electronics for pulse detection Cremat Inc. Cr-11x csp modules, csp housing. <http://www.cremat.com/>, 2019. Accessed: 2019-03-25.
- [42] Ametec Ortec. 673 spectroscopy amplifier and gated integrator. <https://www.ortec-online.com/products/electronics/amplifiers/673>, 2019. Accessed: 2019-03-25.
- [43] Tennelec. *Instruction Manual TC 244 Amplifier*. Tennelec. Accessed: 2019-04-13.
- [44] Fast ComTec. *MCA4 4 Input Multichannel Analyzer 2 Input Multichannel Scaler Manual*. FAST ComTec GmbH. Accessed: 2019-04-13.
- [45] LND. Fission chamber. <https://www.lndinc.com/products/neutron-detectors/3053/>, 2019. Accessed: 2019-03-21.
- [46] F. Issa, A. Khaplanov, R. Hall-Wilton, I. Llamas, M. Dalseth Riktor, S. R. Brattheim, and H. Perrey. Characterization of thermal neutron beam monitors. *Phys. Rev. Accel. Beams*, 20:092801, Sep 2017.
- [47] Mirrotron. Mirrotron. <https://mirrotron.com/en/products/radiation-shielding>, 2019.
- [48] Soo Hyun Byun. Lecture notes in radioisotopes and radiation methodology, chapter 6, 2018. Accessed: 2019-04-03.
- [49] M. Tanabashi, K. Hagiwara, K. Hikasa, K. Nakamura, Y. Sumino, F. Takahashi, J. Tanaka, K. Agashe, G. Aielli, C. Amsler, et al. Review of particle physics. *Physical Review D*, 98(3), 8 2018.
- [50] S.C. Roy and R.E. Apfel. Semi-empirical formula for the stopping power of ions. *Nuclear Instruments and Methods in Physics Research Section B: Beam Interactions with Materials and Atoms*, 4(1):20 – 22, 1984.



EUROPEAN
SPALLATION
SOURCE

brightness



DETECTOR
GROUP
ESS

Sonnig

Source-based Neutron Irradiation Group
Division of Nuclear Physics
Lund University